NASA CR-134593
CASD-NAS-74-005

AN ANALYTICAL STUDY OF REDUCED-GRAVITY PROPELLANT SETTLING

February 1974

by
R. D. Bradshaw
J. L. Kramer

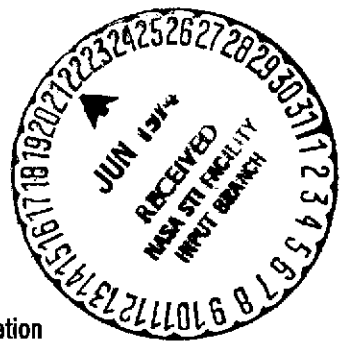

Prepared for
National Aeronautics and Space Administration
LEWIS RESEARCH CENTER
Cleveland, Ohio

Contract NAS3-16772

GENERAL DYNAMICS
Convair Aerospace Division

NASA CR-134593
CASD-NAS-74-006

AN ANALYTICAL STUDY OF REDUCED-GRAVITY PROPELLANT SETTLING

February 1974

by
R. D. Bradshaw
J. L. Kramer

Prepared for
National Aeronautics and Space Administration
LEWIS RESEARCH CENTER
Cleveland, Ohio

Prepared Under
Contract NAS3-16772

Prepared by
GENERAL DYNAMICS CONVAIR AEROSPACE DIVISION
P.O. Box. 80847
San Diego, California 92138

1. Report No.	2. Government Accession No.	3. Recipient's Catalog No.
NASA CR 134593		

4. Title and Subtitle	5. Report Date
AN ANALYTICAL STUDY OF REDUCED-GRAVITY PROPELLANT SETTLING	February 1974
	6. Performing Organization Code

7. Author(s)	8. Performing Organization Report No.
Robert D. Bradshaw James L. Kramer	CASD-NAS-74-005
	10. Work Unit No.

9. Performing Organization Name and Address	11. Contract or Grant No.
Convair Aerospace Division of General Dynamics P.O. Box 80847 San Diego, CA 92138	NAS3-16772
	13. Type of Report and Period Covered
12. Sponsoring Agency Name and Address	Contractor Report
National Aeronautics and Space Administration Washington, DC 20546	14. Sponsoring Agency Code

15. Supplementary Notes

Project Manager, William J. Masica, Chemical Propulsion Division
NASA Lewis Research Center, Cleveland, Ohio 44135

16. Abstract

A study was performed to define full-scale propellant reorientation flow dynamics for the D-1T Centaur fuel tank. A computer code using the Simplified Marker and Cell technique was modified to include the capability for a variable grid mesh configuration. The use of smaller cells near the boundary, near baffles and in corners provides improved flow resolution. The new program, structured in overlay, is more efficient in core usage and is suitable for larger size problems. Three Lewis Research Center drop tower model cases were simulated to verify program validity, two cases without baffles and one case with baffles and geometry identical to D-1T Centaur. Flow phenomena using the new code successfully modeled drop tower data. Flow trajectories off the baffles exhibited dependence on initial fluid location in relation to the baffle and on initial flow velocity. Two full-scale D-1T Centaur cases were then simulated using parameters based on the Centaur D-1T Proof Flight. These flow simulations indicated the time to clear the vent area and an indication of time to reorient and collect the propellant. The results further indicated the complexity of the reorientation flow and the long time period which is required for settling. These full-scale numerical results agreed with the extrapolation from drop tower data.

17. Key Words (Suggested by Author(s))	18. Distribution Statement
Reduced Gravity, Settling, Centaur, Incompressible Fluid Mechanics, Marker and Cell	Unclassified - Unlimited

19. Security Classif. (of this report)	20. Security Classif. (of this page)	21. No. of Pages	22. Price*
Unclassified	Unclassified	58	$3.00

* For sale by the National Technical Information Service, Springfield, Virginia 22151

FOREWORD

This computer development and application study was conducted by General Dynamics Convair Aerospace Division, San Diego Operation, under NASA Contract NAS3-16772. The research was accomplished under the direction of the NASA Project Manager, Mr. William J. Masica, NASA-Lewis Research Center. The study was completed under the direction of Convair project leader, Dr. Robert D. Bradshaw with the Scientific Programming assistance of Mr. James L. Kramer. The author wishes to acknowledge the direction of Mr. Masica, the initial efforts of Mr. W. S. Betts (project leader July 1972 to September 1972) and the initial programming assistance of Mr. A. J. Bowker.

ABSTRACT

A study was performed to define full-scale propellant reorientation flow dynamics for the D-1T Centaur fuel tank. A computer code using the Simplified Marker and Cell technique was modified to include the capability for a variable grid mesh configuration. The use of smaller cells near the boundary, near baffles and in corners provides improved flow resolution. The new program, structured in overlay, is more efficient in core usage and is suitable for larger size problems. Three Lewis Research Center drop tower model cases were simulated to verify program validity, two cases without baffles and one case with baffles and geometry identical to D-1T Centaur. Flow phenomena using the new code successfully modeled drop tower data. Flow trajectories off the baffles exhibited dependence on initial fluid location in relation to the baffle and on initial flow velocity. Two full-scale D-1T Centaur cases were then simulated using parameters based on the Centaur D-1T Proof Flight. These flow simulations indicated the time to clear the vent area and an indication of time to reorient and collect the propellant. The results further indicated the complexity of the reorientation flow and the long time period which is required for settling. These full-scale numerical results agreed with the extrapolation from drop tower data.

TABLE OF CONTENTS

LIST OF FIGURES

LIST OF FIGURES, Contd

LIST OF TABLES

SUMMARY

For restart missions with upper-stage vehicles, a requirement exists to reorient the propellant to the aft end of the tank and to vent prior to engine start. For the Centaur D-1T vehicle, settling motors provide the thrust to reorient the propellant from its stable low-gravity orientation which is in the forward end of the tank due to drag. Analytical techniques using Marker and Cell methods to solve the equations of motion are available to model the flow behavior during reorientation.

During the reorientation maneuver, the flow dynamics of the residual liquid are of interest as they define the time at which the liquid clears the top area of the tank so that venting can occur. The flow pattern and any geyser activity influences this value of time for venting. A second value of time of interest in the reorientation maneuver is the time to achieve a collected state for the propellant. At this time the propellant has flowed to a new stable location in the tank which satisfies the new acceleration field. Since sloshing continues as well as bubble clearing after this collected state is attained, the liquid is not considered settled until a considerable time after collection occurs.

The first phase of this study involved the modification of a previous version of a Simplified Marker and Cell (SMAC) computer code to more effectively analyze propellant reorientation. The new computer code was structured in overlay to reduce core storage and improve program efficiency. The major task in this phase was to modify the code to a variable grid capability so that better resolution of thin boundary layer flow could be obtained near walls, baffles and in corner areas. The variable grid concept permits each cell to have one or two neighbors per side. Thus considerable variation in grid mesh is available. This computer program modification required special treatment in areas of neighbor definition, velocity equation differencing techniques and pressure interpolation. Finally, the acceleration input was redefined as time-dependent in the axial direction for solution of axi-symmetric problems in cylindrical coordinates. The new computer code, ERIE, retained the capability for arbitrary boundaries and surface tension.

Five propellant settling cases were simulated, three drop tower model cases which were scale models of Centaur fuel tanks and two full-scale D-1T Centaur fuel tanks. The first two drop tower cases which were analyzed did not contain baffles; the former verified the modifications of the code involving variable grid logic by a comparison with an earlier 20 percent liquid residual settling case. Results for leading edge velocities and lower bulkhead flow indicated satisfactory modeling. The second model case with 65 percent liquid utilized the time-dependent gravity field capability to examine impulsive settling; this case encountered convergence problems which were not resolved. The final drop tower case demonstrated the use of arbitrary boundaries to model baffles; this case confirmed the settling flow patterns with baffles as well as establishing geometry for the D-1T full-scale cases. Some geyser activity occurring in the drop

tower tests was not simulated with code ERIE; different initial conditions may explain this.

Two full-scale cases were simulated to determine settling flow phenomena prior to venting for third and fourth burns of D-1T Centaur proof flight. A settling acceleration equivalent to Bond numbers of 200 and 450 were used in the 152.4 cm radius tank. With the 20 percent liquid residual case, the vent area was cleared in 55 seconds and the liquid was collected by 120 seconds. In the 70 percent liquid residual case, the vent cleared at 120 seconds and propellant was essentially collected by 155 seconds. Some geysering behavior was observed in this latter simulation. However, no impingement was detected on remaining liquid which is clearing from the upper vent area. The baffles were shown to be very effective in reducing geysering activity. Numerical results agreed with the extrapolation from drop-tower data. However, the importance of both initial propellant location and the magnitude of full-scale settling acceleration on flow trajectories off the baffle was demonstrated.

The promising results of the simulation of full-scale flow phenomena indicate the potential for analyzing fluid motion in reduced gravity environments, for modeling flow behavior around the Centaur LOX tank thrust barrel, for looking at interface stability and for successfully demonstrating time-dependent acceleration reorientation flow.

1.0 INTRODUCTION

During low-gravity vehicle coast, drag forces can cause the propellant to move in the tank and assume a stable configuration in a location away from the outlet. With the D-1T Centaur, a typical upper-stage vehicle, two or four 6 lb thrusters are used to settle the propellant aft in the tank for engine venting and restart. Estimated settling times to date have generally been determined from empirical methods growing out of drop tower model results. However, the use of excessive propellant because of some lack of confidence in understanding the flow phenomena associated with the settling operation results in a loss of payload capability.

The Simplified Marker and Cell technique offers a method whereby the solution of the equations of motion affords a computer simulation approach to predicting settling flow. An acceleration field equivalent to that resulting from the thrusters is applied to the fluid in the tank. The movement of the fluid is described by marker particles moving within a grid mesh indicating the location of full and surface cells and by velocity vectors defined at grid cell mesh locations which indicate the strength of the velocity field. The pressure field defines the force on all boundary objects in the grid mesh. The computer codes in existance prior to the start of this study did not provide adequate grid mesh resolution. It was determined that to model boundary layer flow, to model flow in a corner where a bulkhead and a cylindrical wall meet, and to model baffles in a tank, an improved computer model with a variable grid mesh was required. An existing program was modified extensively to meet these requirements. This program was then verified with the simulation of three drop tower model settling problems with D-1T geometry with and without baffles. The application to full-scale problems was demonstrated with settling predictions for the D-1T Centaur Proof Flight venting sequences with 70 and 20 percent liquid residuals. This type of simulation has potential for analysis of several fluid motion problems during docking, engine shutdown, and in preparation for engine restart.

2.0 COMPUTER CODE DEVELOPMENT

The computer code developed under this study is named ERIE (Ref. 1). It is a modified version of the program HOPI developed under a similar investigation (Ref. 2 and 3). The primary modification is the capability to use a variable-size rectangular grid mesh. The code was developed in overlay structure to minimize core storage. Both this program and HOPI are outgrowths of the SMAC (Simplified Marker and Cell) method, the ZUNI Code (Ref. 4), for solution of the dynamic behavior of an incompressible fluid. This method uses a grid mesh of cells with movement of marker particles to indicate fluid location. This current version of the program includes arbitrary boundaries, surface tension and surface marker particles, and a time-dependent gravity field. The development and verification of this code with variable grid, overlay structure, and time-dependent acceleration field completed one objective of the study. The second objective, the simulation of five settling cases, will be discussed in the next section.

The SMAC method is a numerical finite difference technique for solution of the Navier-Stokes equations of motion for incompressible viscous fluid flow. The method solves the complete Navier-Stokes equations giving a time-dependent solution. The method is applicable to confined flow or free surface flow. The SMAC method overlays the fluid with a two-dimensional rectangular grid mesh in either rectangular or cylindrical coordinates. Horizontal velocities are defined at the midpoints of each side of each rectangular element while vertical velocities are defined at the midpoints of the top and bottom sides. Finite velocities are defined only for cells which are full or surface; the latter being those next to an empty cell. Various designations are given to other cells in the grid depending on their location and function as shown in Figure 1. Velocities are calculated each time-step for each full and surface cell. Velocities satisfy tangential and normal stresses on surface cells.

A pressure field is defined throughout the fluid with the pressure defined at each cell center of a full cell. The pressures on surface cells are interpolated to satisfy the normal stress condition plus a surface tension pressure force. The calculation proceeds with a calculation over all full and surface cells during which velocities are set independent of pressure and the divergence requirement. These velocities do assure that vorticity is satisfied at each cell corner. The iteration procedure in the SMAC code then modifies these velocities to minimize divergence over all cells by adjusting the pressure on each cell by an incremental amount. The iteration is complete when a specified convergence criteria is satisfied based on a measure of the pressure change which is proportional to divergence.

ARB An OB cell which has a fluid particle within $\epsilon \cdot DR$ of the arbitrary boundary, where ϵ is the boundary sensing parameter and is usually set equal to 0.25.

BND A border cell which is neither COR or EXT.

BOR A cell bordering the interior cells. A border cell is not an interior cell and cannot contain fluid.

BOT A COR cell containing a segment of an arbitrary boundary which has its midpoint and angle being stored in the OB cell just below it.

COR A cell which has a line segment of the arbitrary boundary passing through it, however, fluid area to total cell area fraction is less than 0.25. The fluid area is to the left of the line segment. Also, any cell just outside an OB cell is a COR cell.

EMP The cell is empty (contains no fluid particles).

EOC A cell which is either EMP or COR.

EXT Any cell outside a COR cell.

FUL A cell which contains fluid and has no empty neighbor.

LEF A COR cell containing a segment of an arbitrary boundary which has its midpoint and angle being stored in the OB cell just to the left of it.

OB A cell which has a line segment of the arbitrary boundary associated with it (see COR).

OK An ARB cell that does not contain the intersection of a free surface and the boundary.

RIG A COR cell containing a segment of an arbitrary boundary which has its midpoint and angle being stored in the OB cell just to the right of it.

SNC A cell which is also flagged as FUL or SUR and not COR.

SUR A cell which contains fluid and has at least one neighbor with an empty neighbor not COR or EXT.

TOP A COR cell containing a segment of an arbitrary boundary which has its midpoint and angle being stored in the OB cell just above it.

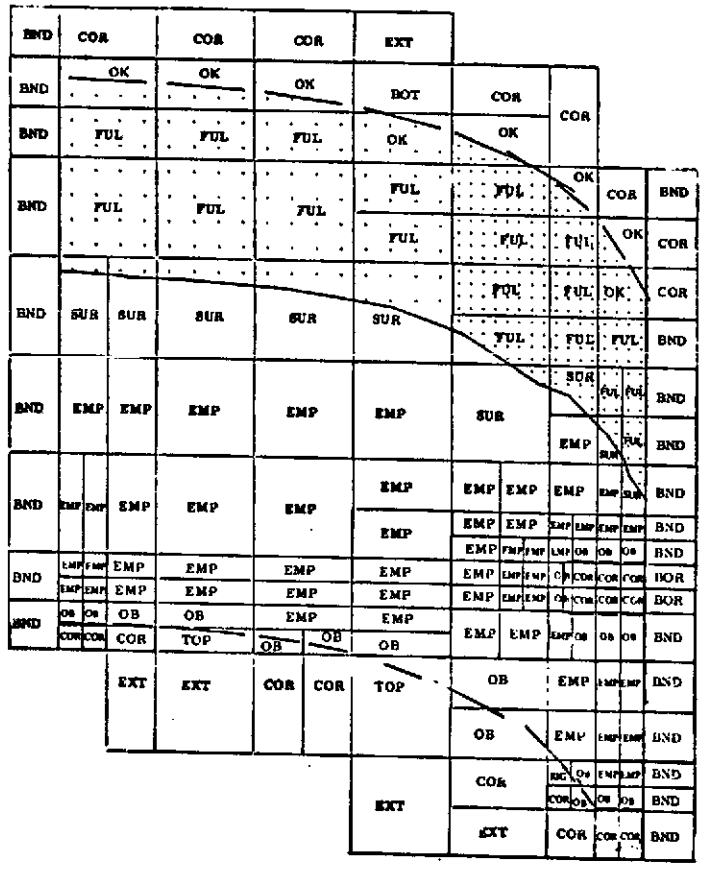

1. All ARB cells are also flagged as ØB.
2. All TØP, BØT, RIG and LEF cells are also flagged as CØR cells.
3. All the above SUR and FUL cells are also flagged SNC.

Figure 1. Variable Grid Network Illustrating Typical Cell Flags

When convergence is satisfied, the velocities calculated above are used to move an array of massless particles which are initially assigned to full cells and move throughout the grid mesh defining both the surface and the fluid location. It is these marker particles which give the method its name, marker and cell. The surface is defined not only by the above criteria for surface cells but also with an array of surface particles which are moved in a similar manner to marker particles. These surface particles also define the magnitude of the surface tension pressure. The graphic output of these particles each time-step and a similar printout of cell-centered velocity vectors are the descriptive output of this method. This is in addition to velocity, pressure, divergence data, and cell flag data which are printed out for each cell. The distance moved by particles in relation to the grid size is the primary determinant of the time-step.

The boundaries to the fluid motion may be rigid or arbitrary. The former follow cell boundaries while the latter represent either straight or curved surfaces and are input completely arbitrarily by a two-dimensional grid-coordinate array. A more detailed analytical development of the above procedures is presented in the following sections.

2.1 EQUATIONS OF MOTION

The computer code ERIE solves the Navier-Stokes equations and satisfies the equation of continuity, i.e., divergence for full fluid cells is zero. The basic differential equations are presented below.

$$\frac{\partial u}{\partial t} + \frac{1}{r^{\alpha}} \frac{\partial r^{\alpha} u^2}{\partial r} + \frac{\partial uv}{\partial z} = -\frac{\partial \phi}{\partial r} + g_r(t) + \upsilon \frac{\partial}{\partial z} \left(\frac{\partial u}{\partial z} - \frac{\partial v}{\partial r} \right) \tag{1}$$

$$\frac{\partial v}{\partial t} + \frac{1}{r^{\alpha}} \frac{\partial r^{\alpha} uv}{\partial r} + \frac{\partial v^2}{\partial z} = -\frac{\partial \phi}{\partial z} + g_z(t) - \frac{\upsilon}{r^{\alpha}} \frac{\partial}{\partial r} \left[r^{\alpha} \left(\frac{\partial u}{\partial z} - \frac{\partial v}{\partial r} \right) \right] \tag{2}$$

$$D = \frac{1}{r^{\alpha}} \frac{\partial r^{\alpha} u}{\partial r} + \frac{\partial v}{\partial z} = 0 \tag{3}$$

The pressure ϕ is normalized with fluid density and has units L^2T^{-2}. The above equations are applicable to rectangular coordinates when $\alpha = 0$ and apply to cylindrical coordinates when $\alpha = 1$. The SMAC code utilized ZIP-differencing techniques to solve the above equations using variables identified at specific cell locations. The modification of that code to variable grid, VGSMAC, introduced limitations on the differencing techniques. It can be shown that for the difference techniques to be accurate the distances over which the uv product terms are determined must be equal. Since this condition would not necessarily exist in a variable grid, a restriction must be placed on the location points for the definition of cell velocities in solving the equations. The above equations are presented in difference form in Equations 4, 5, and 6. Note that tentative velocities, $\tilde{u}$ and $\tilde{v}$, are defined by these equations which are velocities that

are independent of the pressure field. The velocity and grid locations for these calculations are shown in Figure 2 for a uniform grid. If a variable grid cell structure is in use, the velocity locations and distances remain the same relative to cell N with the velocities outside cell N obtained by interpolation (Ref. 1).

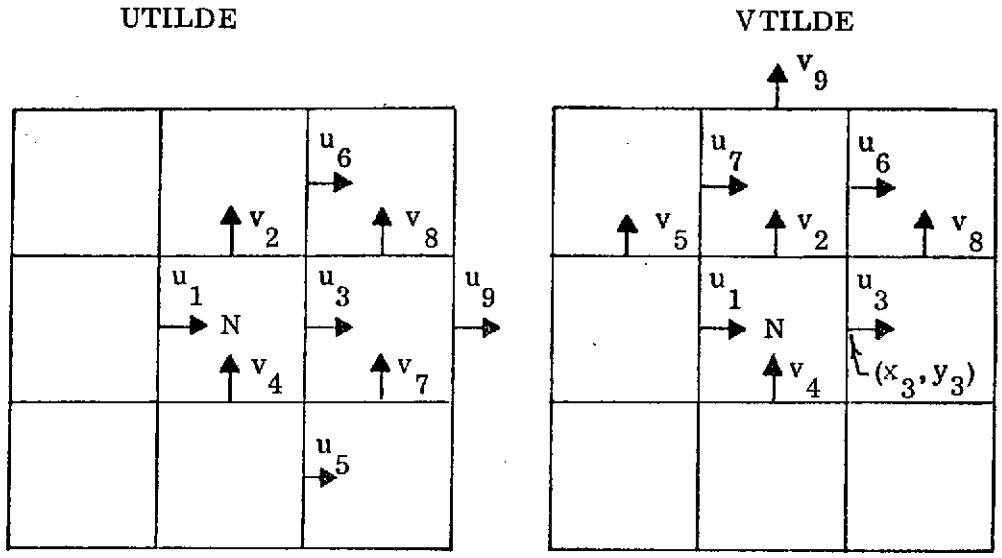

Figure 2. The Definition of Cell Variables in VGSMAC for Tilde Velocity Calculation

The equations below are in the cylindrical coordinate system but can be modified to rectangular coordinates with the substitution of 1 for R_N, R_1, R_3, R_9. The radial or r direction is x and the vertical or z direction is y. A $\tilde{u}_R$ is calculated for all full or surface cells which have no empty right neighbors, and $\tilde{v}_T$ is calculated for all full or surface cells which have no empty top neighbors. The equations, used with ZIP-type differencing using the terminology defined in Figure 2, are

$$\tilde{u}_R^{n+1} = u_3 + \delta t \left\{ \frac{u_3}{RIP_N} \left[\frac{R_N u_1 - R_9 u_9}{.5(x_9+x_3) \quad -x_2} \right] + \frac{1}{\delta z_N} \left[\left(\frac{(y_4-y_5)\, u_3 + (y_3-y_4)\, u_5}{y_3-y_5} \right) \right.\right.$$

$$\times \left(\frac{(x_3-x_2)v_7 + (x_7-x_3)v_4}{x_7-x_3} \right) - \left(\frac{(y_2-y_3)u_6 + (y_6-y_2)u_3}{y_6-y_3} \right) \left(\frac{(x_3-x_2)v_8 + (x_8-x_3)v_2}{x_8-x_2} \right) \left. \right]$$

$$\left. + g_r + \frac{\nu}{\delta z_N} \left[\left(\frac{u_6-u_3}{y_6-y_3} - \frac{u_3-u_5}{y_3-y_5} \right) - \left(\frac{v_8-v_2}{x_8-x_2} - \frac{v_7-v_4}{x_7-x_4} \right) \right] \right\} \qquad (4)$$

where

R_N in rectangular coordinates = 1; in cylindrical = .5 $(x_1 + x_3)$

RIP_N in rectangular coordinates = 1; in cylindrical = x_3

R_9 in rectangular coordinates = 1; in cylindrical = .5 $(x_3 + x_9)$

$$\tilde{v}_T^{n+1} = v_2 + \delta t \left\{ \frac{v_2(v_4 - v_9)}{.5(y_9+y_2) - y_3} + \frac{1}{R_N \delta r_N} \left[RIP_{NL} \left(\frac{(y_2-y_3)u_7 + (y_7-y_2)u_1}{y_7-y_3} \right) \right. \right.$$

$$\times \left(\frac{(x_1-x_5)v_2 + (x_2-x_1)v_5}{x_2-x_5} \right) - RIP_N \left(\frac{(y_2-y_3)u_6 + (y_6-y_2)u_3}{y_6-y_3} \right) \times \left. \left(\frac{(x_3-x_2)v_8 + (x_8-x_3)v_2}{x_8-x_2} \right) \right]$$

$$+ g_z - \frac{\upsilon}{R_N \delta r_N} \left[RIP_N \left(\frac{u_6-u_3}{y_6-y_3} - \frac{v_8-v_2}{x_8-x_2} \right) - RIP_{NL} \left(\frac{u_7-u_1}{y_7-y_1} - \frac{v_2-v_5}{x_2-x_5} \right) \right] \Bigg\} \qquad (5)$$

where RIP_{NL} in rectangular coordinate = 1; in cylindrical = x_1.

$$D_N^{n+1} = \frac{u_3 R_3 - u_1 R_1}{R_N \delta x} + \frac{V_2 - V_4}{\delta y_N} \qquad (6)$$

This tentative field of advanced-time velocities, $\tilde{u}$ and $\tilde{v}$, are determined independent of the pressure field. These values are modified by the pressure field in the iteration scheme to define final velocities. The tentative velocities do not satisfy continuity, i.e., divergence. Correct velocity boundary conditions assure that the final velocity field contains the correct vorticity at every interior point in the field. The tentative velocities are modified in the iterations to their final values so as to preserve the vorticity at every point. In differential form, the equation for transport of vorticity, ω, is independent of the pressure, so that any field of pressure inserted into the Navier-Stokes equations will assure that the resulting velocity field carries the correct vorticity. The subscripts in Equations 5, 6, and 7 refer to position in the finite-difference mesh (see Figure 2), and the superscript n counts time cycles. The true pressure, ϕ, has been replaced by the arbitrary field, ψ, and accordingly the new-time velocities are marked with tildes. Later when divergence is satisfied and final velocities are calculated, the true pressures are defined for full and surface cells.

A finite-difference approximation to the vorticity is

$$\omega_{N(r_3, z_2)}^n \equiv \frac{u_6^n - u_3^n}{\delta z} - \frac{v_8^n - v_2^n}{\delta r} \qquad (7)$$

with centering at cell corners. The form of Equations 1 and 2 result in a transport expression for $\omega_N(r_3, z_2)$ which, like the differential equation, is independent of the ψ field. Accordingly, the calculations of the tilde velocities assures that the vorticity at every internal mesh corner point is correct, independent of the choice of ψ, the arbitrary pressure field. For purely explicit calculations, which are acceptable for Reynolds numbers greater than about unity, SMAC vorticity diffusion from the wall is correct, because the tilde velocities are based entirely upon the final velocities from the previous cycle, which do agree with the proper wall vorticity.

A cell is flagged as a surface (SUR) cell when it contains fluid marker particles and it has at least one adjacent neighboring cell which is flagged empty. Marker particles do not perform any function that may be present. On free surfaces the tangential stress condition is

$$\frac{\partial u}{\partial z} + \frac{\partial v}{\partial r} = 0$$

so that u_6 is determined by the equation

$$u_6 = u_3 - \frac{\delta z}{\delta r}(v_8 - v_2) \tag{8}$$

This assures that the tangential viscous momentum flux vanishes when calculated by Equation 1 for u_3.

In addition, the normal stress condition is

$$\phi_N = \phi_N \text{ (applied)} + \frac{2\upsilon}{\delta z}(v_2 - v_4) \tag{9}$$

The applied part of the pressure is specified according to the requirement of the problem while the viscous part assures that there is otherwise no net flux of normal momentum through the surface. It is important that the normal stress condition be placed on the free surface rather than at the center of the surface cell.

The tentative velocities are calculated for all full and surface cells without the pressure contribution. These tilde velocities are determined before the final iteration scheme. Then, the pressure in each full cell is modified to minimize the summation of a normalized divergence for all full cells. Thus, tentative velocities are modified by Equations 10 and 11 in the iteration scheme

$$u = \tilde{u} + \delta t \frac{\partial \psi}{\partial r} \tag{10}$$

$$v = \tilde{v} + \delta t \frac{\partial \psi}{\partial z} \tag{11}$$

The viscosity coefficient υ used in Equations 1 and 2 is the sum of a kinematic molecular viscosity and a turbulent viscosity.

$$\upsilon = \upsilon_{\text{molecular}} + \upsilon_{\text{turb}}$$

The molecular viscosity is an input quantity and is a fluid property. The turbulent viscosity coefficient is calculated internally in the program as indicated below.

$$\upsilon_{\text{turb}} = \text{TURB} \times \ell^2 \max \left(\left| \frac{\partial v}{\partial r} \right|, \left| \frac{\partial u}{\partial z} \right| \right) \tag{12}$$

where

$$\ell = \begin{cases} \text{DR if } \left| \frac{\partial v}{\partial r} \right| > \left| \frac{\partial u}{\partial z} \right| \\ \text{DZ if } \left| \frac{\partial u}{\partial z} \right| > \left| \frac{\partial v}{\partial r} \right| \end{cases}$$

and TURB is an input quality which was held constant at 0.05 (Ref. 2).

This expression for turbulent viscosity is of the form predicted by both Prandtl's mixing-length theory and Taylor's vorticity transport theory. While other expressions for predicting the turbulent viscosity do exist, the above was selected due to its wide acceptance and simplicity.

A turbulent viscosity is calculated in a cell containing fluid when at least two of its adjacent neighboring cells also contain fluid. The criteria of requiring fluid in adjacent fluid cells is needed so that $\partial v/\partial r$ and $\partial u/\partial z$ can be calculated.

For the reorientation flow cases examined in this study (Section 3) the magnitude of the local turbulent viscosity coefficient was at least an order of magnitude greater than the molecular viscosity coefficient for most of the problem duration. This indicates that the viscosity coefficient used in Equations 1 and 2 is mainly a result of the turbulent viscosity coefficient.

2.2 ERIE COMPUTER CODE

This section describes in detail the variable grid VGSMAC calculational cycle in the framework of ERIE. The code ERIE contains a number of features that make it a useful analytical tool for fluid dynamic studies. In particular,

a. The code is written in FORTRAN IV for the CDC-6400 computer in overlay structure and interfaces with the SC-4020 plotter to provide particle and velocity vector plots.

b. The code can be used with either cylindrical or rectangular geometry. Axisymmetric flow can be computed in a cylindrical geometry mode.

c. Grid mesh size may be varied for different areas of the model, i.e., a variable grid. The size of the computing mesh can be changed from problem to problem, including both the number and size of cells and the number of particles. The setup allows for different initial conditions and particle resolution in specified regions of the mesh. A scaling feature provides for model and full-scale simulation by changing only one variable.

d. Various boundary conditions are available, along with an obstacle. Both curved and straight wall boundaries can be used.

e. This code can calculate both free-surface and confined flows. Surface conditions include a surface tension force.

f. Gravitational effects in rectangular coordinates may be included in any orientation and are time-dependent. In cylindrical coordinates, only the axial gravity force is appropriate due to symmetry; it is also time-dependent.

The above features will be discussed in further detail in the following sections.

2.2.1 OVERLAY STRUCTURE. A significant savings in costs resulted from the reduction in core requirements for ERIE with the implementation of overlay structure. The reprogramming for variable grid logic and a capability for fifty percent more cells would have considerably increased core requirements above those required in Reference 2; however in reality, the overlay structure resulted in a reduction in maximum core required. Further, the capability to reduce core for the iteration overlay link (3,0) of the program, where more than half the calculation time is spent in iterating on pressure, brings additional savings on time-sharing computers. The calculations in the basic overlay links are shown in Figure 3.

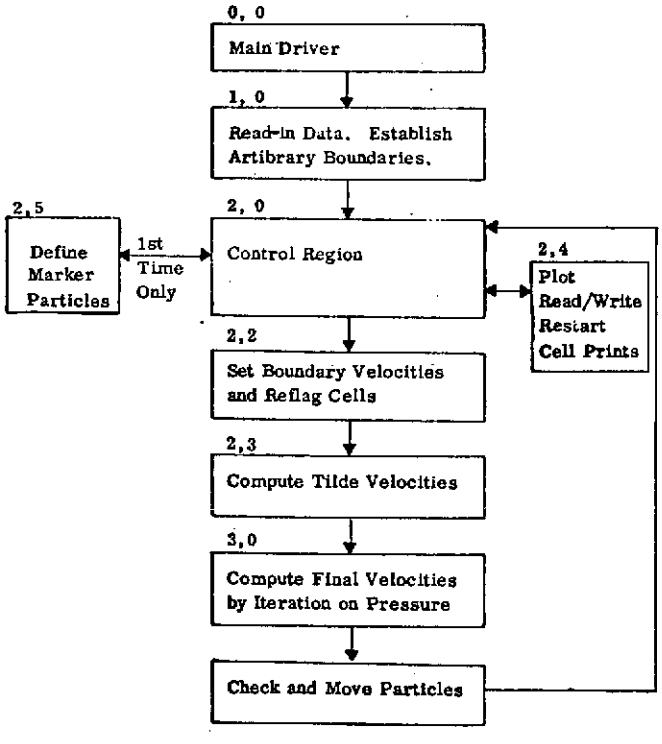

Figure 3. Basic Logic Flow of Overlay for Program ERIE

The capability to generate plot tapes for the S-C 4020 greatly increases the use of the program as an analytic tool. The large amount of data generated can hardly be used without reduction to pictorial form. The marker particle and velocity vector plots are most beneficial in an analysis of flow patterns. A Subroutine ARROW was added to improve the clarity of velocity vector plots, the capability to change the scaling on the velocity vectors also increased their usefulness. A provision is still needed to indicate the magnitude of a unit vector such that comparisons

between times can be made; currently scaling in proportion to the maximum tank velocity makes comparisons between times of lesser value and the vector magnitudes are relative to their own picture. Examples of vector plots appear in Section 3.5.

2.2.2 COORDINATE SYSTEMS. The variable grid version of this program retained the original capability for rectangular coordinates as well as cylindrical coordinates. Only the latter were used in this study. The use of zero for α in Equations 1, 2, and 3 results in a plane coordinate calculation; this option is achieved by setting a single flag .

The cylindrical coordinate system provides for axisymmetric flow. The computing mesh is actually a very thin radial slice with the left boundary equivalent to the centerline as indicated in Figure 4. Each computing cell is a toroid of revolution.

2.2.3 VARIABLE GRID MESH AND CELL FLAGS. Marker and Cell techniques have previously been used to analyze motions of fluids in containers. It was frequently observed that particular regions of the analysis would benefit from a more refined analysis while other regions required only a coarser treatment. The earlier grid limitation implied that the desired refinement was not possible to achieve because of limited storage capacity and accompanying significantly increased costs. Thus, it was recognized that a variable grid concept, that is, the ability to specify one type of refinement or cell structure in one portion of the problem while having different grid structure in other portions, would be a significant advancement in marker and cell capabilities.

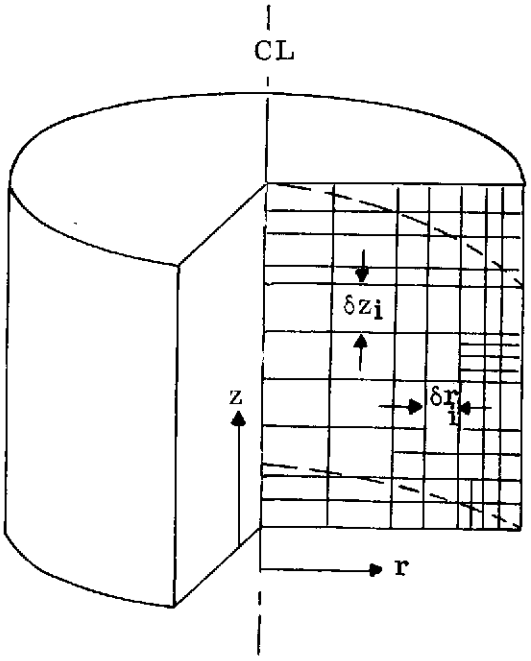

Figure 4. Computing Mesh in Cylindrical Coordinates

Numerous ways of implementing the variable grid concept exist. The method in this contract was chosen as being relatively simple conceptually, while allowing significant flexibility in treating a problem. Each cell is rectangular as it is in the fixed grid model from which the variable grid program was derived. Each interior cell may have either one or two neighbors in each of the four directions, left, top, right or bottom, i.e., a maximum total of eight neighbors. (Border cells of necessity will have no neighbor cells in at least one direction).

The primary cell variables in the ERIE code are velocities u and v on right and top sides, respectively, the pseudo-pressure ψ which is cell-centered except for boundary cells where it is located at the segment midpoint, and the velocity divergence, D, which is satisfied for

full and surface cells and is the convergence criteria on full cells. The calculation of all these variables is compounded by the unequal length of common cell sides. Special provisions were taken to assure cell variables were interpolated at the correct locations outside the cell being determined.

This program computes the above variables throughout a grid mesh in which cells are flagged with one or more flags indicating their fluid state or relation to the boundaries defining the problem. A series of utility subroutines was developed to locate neighbors and to solve for velocities and pressures at specific points in relation to cell N. The ZIP-differencing technique in the Navier-Stokes equations assumes equal spacing of velocity points. These cell flags were defined in Figure 1 where an example is presented of a variable grid configuration with appropriate cell flags indicated. Only the most significant flag is shown on a cell; a cell may be flagged OB, ARB, FUL, OK, and SNC simultaneously.

In ERIE an NBIT function is used to determine if a flag is set for a given cell. Function NBIT interrogates a specified bit of a variable for an on/off indication, this variable contains all the flags for a given cell. To speed up the computation time certain cell flags such as EOC and SNC were developed which represent two or more flags. To further speed up the computation time "G" flags were developed as indicated below.

G = 2 implies a COR cell
G = 3 implies an OK cell
G = 4 implies EMP and not COR or EXT cell
G = 5 implies a BND cell

Determining neighbors' cell flags is more difficult in ERIE than its forerunner HOPI since neighbor combinations and configurations have increased. Criteria had to be established for the many cases where the two neighbors in a given direction carried different flags.

In addition to the mesh of Eulerian cells, VGSMAC employs a set of massless marker particles which are helpful for allowing a visual representation of the fluid. A more essential purpose of these marker particles is to define the position of full and surface cells so that the configuration of the surface can be sensed. Beyond this, the marker particles do not enter into the calculation, but are merely embedded in the fluid and are carried along by it. The particles are inserted at a density per given problem dimension. Since particles primarily impact the flagging procedure, it may be desirable to input denser particle arrays where fluid motion is most rapid or is most interesting, i.e., corners or baffles. Each cycle the marker particles are moved with a distance weighted average of the four nearest u's and of the four nearest v's. This weighting technique differs from the earlier code (Ref. 2, 4) because area weighting could not be applied on a variable grid.

The program input increased in complexity with the introduction of a variable grid in that each cell size is input along with neighbor definition for each cell. Provisions

exist for locating all cells on the grid from boundary cell locations which must be specified. The scaling factor modification for the grid provides a useful method of comparing similar tanks. This was illustrated in this study where a drop tower model (Case 3) and a full-scale D-1T configuration (Case 4) were examined with the same 422-cell grid configuration; the full-scale case being scaled from 7 to 152.4 cm in radius.

2.2.4 BOUNDARY CONDITIONS. In ERIE both straight line and curved wall boundaries can be used. A curved wall is approximated by a series of straight line segments within the grid mesh where each cell that has part of the curved boundary passing through it contains a straight line segment. Each line segment is formed by joining the two points formed where the curved boundary crossed the rectilinear Eulerian boundary of the cell.

For these straight line boundaries, options are available for either freeslip or no-slip boundary conditions. The normal velocity component is set to zero and the gradient in the pressure ψ is set to zero. For freeslip conditions, the tangential velocity is reflected in magnitude and direction into a BND cell, see Figure 4, whereas for non-slip conditions, the velocity is reflected with a negative sign with a zero tangent velocity resulting at the wall.

The ERIE version of the program uses techniques developed by Viecelli for curved-wall arbitrary boundaries (Ref. 7). The curved boundary option offers only freeslip boundary conditions. A series of points are input to specify the curved boundary. These points are a series of coordinates which do not necessarily lie on the grid-mesh lines. To define the arbitrary boundary segments on the grid mesh, successive points are connected by straight lines and their intersections with the grid mesh are determined. Only one straight line per cell is permitted with intermediate points being dropped. The position of this segment within the cell and on the grid mesh is defined by its mid-point and a normal to the segment at the midpoint pointing into the fluid and to the left as one advances along the successive points. The liquid fraction in each cell is calculated, if greater than 1/4 the cell is flagged OB. If less than 1/4 of the cell is liquid, the cell is flagged COR and the program determines to which interior cell the normal points. This interior cell is flagged OB, however if it contains its own boundary segment information, a new segment is generated which spans both these cells, the new normal and midpoint information still being stored in the OB cell. The midpoint may lie physically outside of the OB cell where it is stored. If this occurs, COR cells are also flagged left, right, top, and bottom depending on the direction of the OB cell from the COR cell. This boundary segment construction and flagging procedure is illustrated in Figures 5A and 5B.

Figure 5C indicates certain restrictions in cell geometries which are placed on the variable grid code due to this method of storing boundary cell information. This restriction states that cells containing segments of an arbitrary boundary must be the same length in a common dimension to a cell internal to them such that no instance arises where OB cell information from two cells is required to be stored in one cell.

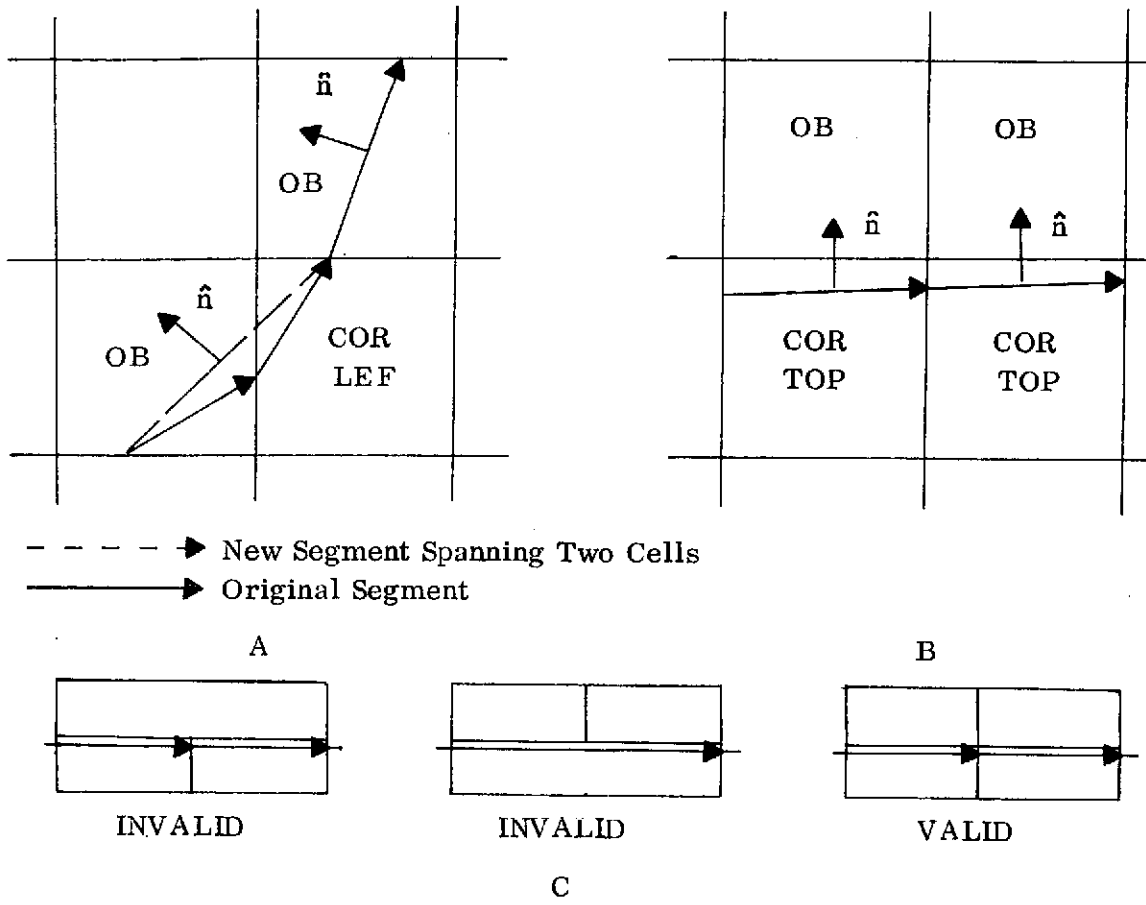

Figure 5. Cell Flags Used With Arbitrary Boundaries

The following relaxation equation is used to compute the pressure in full arbitrary boundary cells

$$\psi_N^{k+1} = \psi_N^k - \frac{RELAX}{\lambda} \left[\left(\vec{V}_M^{n+1} \right)^k \cdot \hat{n} \right]_N \qquad (13)$$

In this equation $\hat{n}$ is the normal defining the boundary segment associated with cell N and $(\vec{V}_M^{n+1})_N^k$ is the liquid velocity at the midpoint of the segment computed with the weighted distance interpolation formula. Clearly $(\vec{V}_M^{n+1})_N^k$ is one of the iterates and must be recomputed each time the pressures and velocities are adjusted. The relaxation parameter and minimum mesh dimension are RELAX and λ, respectively. Note that pressure is not adjusted to satisfy divergence or net flux out of the cell but is adjusted proportional to the velocity directed opposite the normal vector at the segment midpoint. If liquid is flowing across the boundary the pressure is increased until the outflow stops. If liquid is tending to separate from the boundary the pressure is decreased until the liquid flows tangent to the boundary.

In addition to calculating new cell pressures during each iteration cycle one must also recalculate the velocity components. During the iterations the sum of the old velocity

component at time $n\delta t$, the advection and the viscous terms are stored in $\tilde{u}_N$ and $\tilde{v}_N$; these values need to be computed only once. Changes in the new cell velocity iterates then depends only on changes in the gradient of the pressure. In ERIE the pressures of arbitrary boundary cells are located at the boundary midpoint rather than the customary cell center.

In addition to calculating new cell pressures during each iteration cycle one must also recalculate the velocity components. During each iteration the sum of the old velocity component at time $n\delta t$, the advection and the viscous terms are stored in $\tilde{u}_N$ and $\tilde{v}_N$ which need to be computed only once. Changes in the new cell velocity iterates then depend only on changes in the gradient of the pressure iterates. In ERIE the pressures of arbitrary boundary cells are located at the boundary midpoint rather than the customary cell center.

The marker particles, which are typically input at a density of at least four per cell, specify the fluid configuration with an uncertainty much less than the Eulerian mesh width. Therefore some finer criteria other than just the knowledge that a boundary cell contains particles is necessary. We require in addition that

$$(\vec{X}_p - \vec{X}_M) \cdot \hat{n} < \epsilon \lambda$$

where $\vec{X}_p$ is the particle position, $\vec{X}_M$ is the position of the midpoint of the boundary normal, $\hat{n}$ is the boundary normal, and ϵ is some fraction of the cell width λ, typically 1/4. Thus, we do not begin computing a pressure in boundary cells until the particles come within $\epsilon\lambda$ of the boundary segment.

When free surfaces are present we also need to know how to treat cells containing the intersection of curved wall boundaries and free surfaces. The pressure at the intersection point should be equal to the ambient pressure, but because the pressure is defined only on the Eulerian net, it is sometimes not possible to zero the flux at the boundary consistent with vanishing divergence without introducing a pressure. This happens when the angle between the free surface and the boundary is small and the liquid is colliding with a wall, producing a liquid layer on a scale too fine to be resolved by the Eulerian mesh. We define an intersection cell to be one that contains liquid and has one or more empty interior or pressure surface neighbors, and one or more exterior neighbors. When this definition is satisfied, the pressure is set equal to ambient pressure and the velocities are adjusted directly. In most circumstances the liquid in the cell will be part of a much larger mass. When there are one or two liquid neighbors, the velocity components at the sides in contact with the liquid are preserved, and those at the open and boundary sides adjusted to make the velocity tangent at the boundary consistent with vanishing divergence. In the case of one liquid neighbor, the velocities at the opposite cell sides are assumed equal, and the component with both sides open or boundary is adjusted. In either case the flux at the boundary is a linear function of a single variable, and the zero is easily found. If the velocity at the boundary is initially directed away from the boundary, nothing need be done. The

remaining possibility is that there are no liquid neighbors, as happens when a small isolated element strikes the boundary. In this case we set the component of the particle velocity normal to the boundary equal to zero and preserve the tangential component. If a gravitational force is present we accelerate the particle velocities by the component of the gravitational vector tangent to the boundary. This is a free slip condition.

2.2.5 SURFACE TENSION FORCE. An important aspect of surface phenomena in low gravity fields is the surface tension force. At Bond numbers above 10, it is overshadowed in bulk fluid motion by acceleration forces. However the interface behavior may reflect instabilities in the absence of this force. A surface tension calculation is included in the computer code ERIE. It is developed in a manner communicated earlier by Amsden and recently reported (Ref. 8). Five consecutive surface particles are fitted with a quadradic equation. This is used to determine the radius of curvature of the surface. Then a surface tension pressure is defined

$$\psi_{ST} = \sigma\left[\frac{1}{R_{1\sigma}} + \frac{1}{R_{2\sigma}}\right] \tag{14}$$

Pressures are to be specified at each point where the surface intersects lines through cell centers. First, each intersection is found and numbered. When the surface intersects a vertical cell centerline the y-coordinate of the intersection and the pressure at the intersection are found by linear interpolation between the two adjacent surface particles. When the surface intersects a horizontal cell centerline the x-coordinate of the intersection and the pressure are found in a similar way.

For each SUR cell, the intersection point closest to the SUR cell center is determined. All four directions are examined. The program looks from the SUR cell in the direction opposite to the direction of the closest intersection point to find a point at which pressure is defined. This latter pressure and the surface tension pressure at the closest intersection point are used to interpolate a pressure at the center of the SUR cell. In order to define the SUR cell pressure by linear interpolation it is apparent that this latter pressure must lie on the line defined by the intersection point and the SUR cell center. In a variable grid in which a SUR cell may have two neighbors in a given direction, or one neighbor which is longer along the common dimension, a linear interpolation between two adjacent cells (adjacent to the SUR cell) is required to define a pressure at a point to be used in the definition of the pressure of the SUR cell as shown in Figure 6.

The pressure at the center of a SUR cell is computed using the information developed above. The following expression is used

$$\psi_N = (1-\eta)\,\psi_F + (\psi_{ST} + \psi_{NS})\,\eta \tag{15}$$

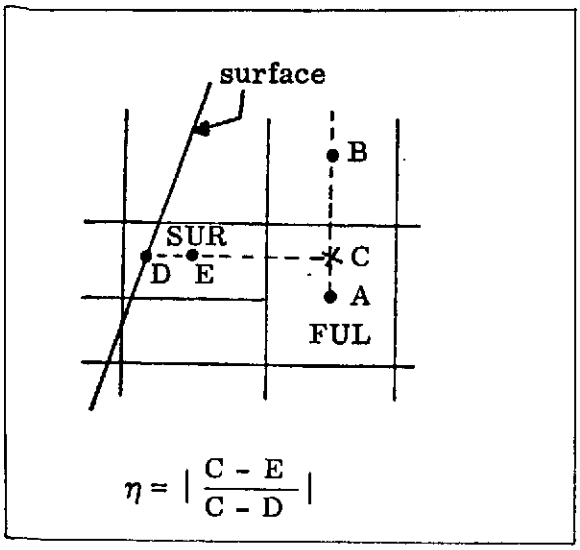

Figure 6. Surface Tension Pressure Solution

in which

ψ_N = the pressure at the center of the SUR cell

ψ_F = the adjacent FUL cell pressure (e.g. point C in Figure 6)

ψ_{ST} = surface tension pressure at the closest intersection point as described above

ψ_{NS} = normal stress pressure

$$\eta = \left| \frac{D_{\text{full cell - surface cell}}}{D_{\text{full cell - surface intersection}}} \right|$$

The value of η is confined to $0.667 \leq \eta \leq 2.0$ to insure only pressures from nearly full cells are used. Equation 15 is used so that when the regular VGSMAC formulas are used for computing velocities in FUL cells adjacent to SUR cells, the desired pressure is simulated at the surface rather than at the center of the SUR cell.

2.2.6 GRAVITATIONAL EFFECTS. One of the study requirements was to implement a time-dependent acceleration field into the code. A time look-up table is used with the acceleration field input in both horizontal and vertical directions in the rectangular coordinate version. In cylindrical coordinates, only an axial time-dependent acceleration force is available due to symmetry considerations. The solution for the tilde velocities uses the current acceleration field information.

2.2.7 TIME-STEP. The procedure for calculation of maximum time-step formerly used in HOPI (Ref. 2) has been modified. The same two stability and two accuracy criteria apply, however now length dimensions (DRSTEP, DZSTEP) are selected equal to the average of the cell mesh sizes; this may exceed the accuracy criteria of the smallest cells. This results in an acceptable time-step selection. The former procedure of halving or doubling the requested time-step has been discarded as inefficient. The new program is much more efficient in using the maximum calculated time-step with the exception that when a print interval time is exceeded the time-step is dropped to the print time. To avoid an extremely small step in this latter case, the criteria is relaxed that a step to a print cycle may exceed the calculated time-step by forty percent.

The first stability criteria exists to satisfy conditions imposed by the differencing technique.

$$\delta t \leq \frac{(DRSTEP)^2 (DZSTEP)^2}{4 \upsilon [(DRSTEP)^2 + (DZSTEP)^2]} \tag{16}$$

The second stability criteria exists to satisfy "Courant" condition and uses the wave speed and fluid depth

$$\delta t \leq \frac{2 * DRSTEP * DZSTEP}{(DRSTEP + DZSTEP)\, c} \tag{17}$$

where c is the wave speed. In the case of zero surface tension, in this study, c is equal $\sqrt{g_z h}$ where h is the liquid height. This stability criteria was not a limiting value during this study. With active surface tension, $c = \sqrt{gh + 2\pi\beta/3 \cdot DRSTEP}$. The third and fourth restrictions are related to accuracy so that a particle does not move across an entire cell in a time-step. The accuracy criteria were the limiting criteria during this study.

$$\delta t \leq \frac{DRSTEP}{2u_{max}} \tag{18}$$

$$\delta t \leq \frac{DZSTEP}{2v_{max}} \tag{19}$$

To insure that particles do not move across an arbitrary boundary during a time step, the particle sensing parameters are included

$$\delta t \leq DRSTEP \times 2 \times \epsilon / u_{max} \tag{20}$$

$$\delta t \leq DZSTEP \times 2 \times \epsilon / v_{max} \tag{21}$$

where ϵ is the boundary sensing parameter. This latter criteria is only used when the fluid is going toward the boundary (not parallel to or away from the boundary).

2.2.8 CONVERGENCE CRITERIA. The iteration scheme continues to adjust the pressure throughout the fluid, i.e. the FUL and OK cells, until the convergence criteria has been satisfied. Recall that tilde velocities are adjusted by the pressure gradient to obtain a velocity distribution which is tested for divergence. Convergence criteria is tested against the sum of the normalized divergence over all cells rather than the divergence of a single cell which would be a more stringent requirement. The tilde velocities are modified into final velocities for the cycle in a way that will preserve the vorticities that have been correctly implanted into the fluid, but in the case of non-ØK cells will now bring the divergence to zero, while in the case of ØK cells will cause the fluid to flow parallel to the arbitrary boundary. At each iteration, a delta pressure is determined for each FUL and ØK cell. New velocities are then computed for that cell as a function of the newly defined pressure before proceding to the next cell. When all

cells have been treated in this fashion, a test is made to see if this pressure field resulted in convergence. If not, the procedure is repeated for another iteration.

At each iteration, k, the change in pressure for FUL and ØK cells is a function of the quantity D (D ≡ divergence for FUL cells) which is computed for all FUL and ØK cells according to the following expressions.

D Calculation for FUL Cells:

$$D_N^{k+1} = \frac{1}{r_N \delta r_N}\left[RIP_N u_N^k - RIP_{NL} u_{NL}^{k+1}\right] + \frac{1}{\delta z_N}\left[v_N^k - v_{NB}^{k+1}\right] \tag{22}$$

D Calculation for ØK Cells:

$$D_N^{k+1} = \frac{DN\emptyset RX_N * UK_N + DN\emptyset RY_N * VK_N}{MAX\ (\delta r_N,\ \delta z_N)} \tag{23}$$

where UK_N and VK_N are the u and v components of the velocity at the midpoint of the boundary segment associated with cell N.

The pressure iteration proceeds through the cells in the order in which they were input. Only one matrix is used for ψ, so that the program uses the latest values (iteration number k+1) for velocities whose index is smaller than that of cell N and old values (iteration number k) for those velocities whose index is greater than N.

The pressure of cell N at the end of k+1 iterations is then defined by

$$\psi_N^{k+1} = \psi_N^k - \xi_N D_N^{k+1} \tag{24}$$

where ξ_N is a relaxation parameter defined by

$$\xi_N = \frac{ALP\ \{[MIN\ (\delta r_N,\ \delta z_N)]^2\}}{\delta t} \tag{25}$$

where ALP is an input variable. It was observed that the relaxation parameter acts in opposition to a decrease in time-step. This behavior was a considered source of difficulty in the impulsive-g case where convergence was not achieved.

$$\left[\frac{\sum_{N=1,NCELL} TEMP^2}{\sum_{N=1,NCELL} (\psi_N - TEMP)^2}\right]^{1/2} < EPS \tag{26}$$

where TEMP = $\xi \times D_N$ for FUL cells has been satisfied for all FUL cells. Here EPS is usually on the order of $8 \times 10^{-4} \times \text{MIN}\ (\delta r_N^{1/2},\ \delta z_N^{1/2})$, (Ref. 7).

2.3 COMPUTER CODE VERIFICATION

The computer code was verified with an investigation of a small settling problem. The cell structure was formulated to checkout various geometry aspects. Driver programs had been set up previously to verify individual velocity and pressure interpolation subroutines. The cell structure was also selected with the provision to change the problem with the addition of an obstacle, a baffle. The grid configuration along with marker particle and velocity vector plots are shown in Figures 7 and 8. The grid includes the baffle in this instance. A choice had to be made to use either fixed boundaries or the arbitrary boundary approach for the baffle. Since arbitrary boundaries make necessary adjustments to velocities adjacent to them, this technique was preferred and did prove successful. The arbitrary boundaries also offer a wider flexibility in size, shape and dimensions.

The small test case problem, a 7×8.5 cm grid mesh of 173 cells, was first run without the baffle. Fluid properties for FC-78^{O} (a fluorocarbon solvent of Minnesota Mining and Manufacturing Co.) were used including a kinematic surface tension coefficient of 7.67 cm^3/sec^2. An impulsive-g case was examined in which the acceleration field, initially -70 cm/sec^2, was dropped to +0.001 cm/sec^2 at 0.30 seconds. The pressure field in the liquid did adjust and the problem continued on smoothly to 0.475 seconds without a noticeable perturbation in iterations. At 0.475 seconds the flow had turned the lower right corner and was moving across the lower bulkhead. Results appear in Figures 7B and 8B. At each time step, velocities, pressures, and flagging were carefully examined to insure proper operations. Minor modifications were required during this effort to program logic. The surface tension pressures were verified during this checkout and although minor changes in logic were required, the values calculated were verified to be correct.

The problem was then restarted at zero with two modifications, the baffle was added using arbitrary boundary logic and the particle density was increased in the area above the baffle. This problem was run to 0.267 seconds and demonstrated satisfactorily that arbitrary boundaries can be used for baffle simulation. The marker particle and velocity vector plots at the end of the problem, time 0.265 sec, are shown in Figures 7C and 8C. With this checkout of the program completed, the study moved on to simulation of the drop tower model cases. These results are discussed in Section 3.

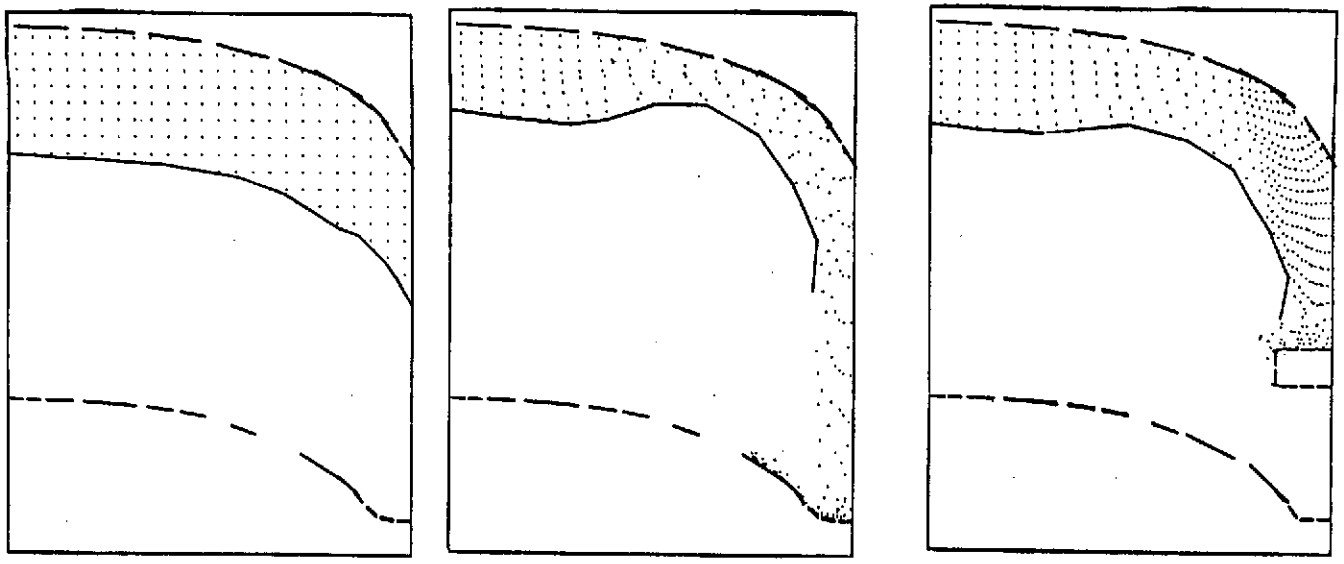

A. T = 0.0 SEC B. T = 0.475 SEC C. T = 0.264 SEC

Figure 7. Marker Particle Plots for Test Case Settling Problem

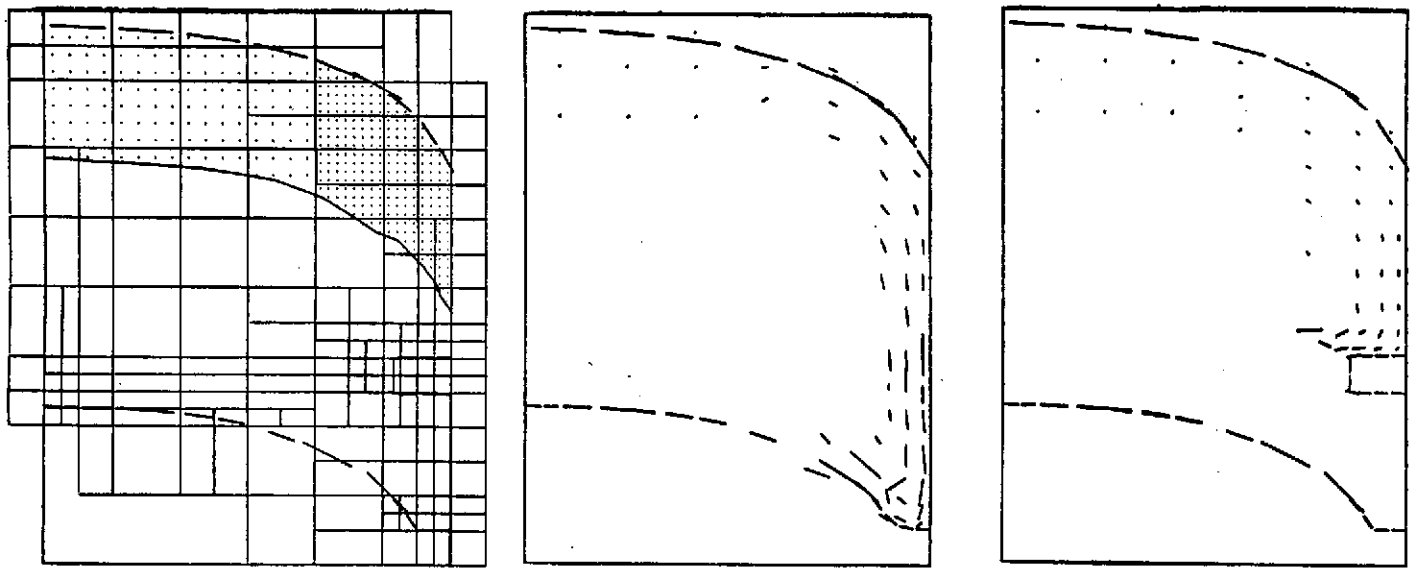

A. T = 0.0 SEC B. T = 0.475 SEC C. T = 0.264 SEC

Figure 8. Velocity Vector Plots for Test Case Settling Problem

3.0 SIMULATION MODELING

The computer model described in Section 2.0 was used to analyze propellant settling flow phenomena for the three model cases and two full-scale D-1T Centaur hydrogen fuel tanks. The results of these five cases are discussed in this section. Results of three of the cases are compared with excerpts from a film presentation of drop tower results obtained at NASA/Lewis Research Center. A discussion of modeling problems encountered during this phase of study is included. A summary of pertinent data for the five cases is shown in Table I.

TABLE I. FLUID AND PROPERTY DATA FOR FIVE MODEL CASES

	Radius cm	Fluid	Baffles	Liquid %	Bond Number, initial	Acceleration cm/sec^2	υ cm^2/sec	σ cm^3/sec^2
Case 1	7.0	FC-78[2]	No	20	10	-70.0	0.00477	0
Case 2	5.5	Ethanol	No	65	15	-73.5[1]	0.01520	0
Case 3	7.0	FC-78[2]	Yes	20	15	-69.6	0.00477	0
Case 4	152.4	LH_2	Yes	20	0	-0.643	0.00192	0
Case 5	152.4	LH_2	Yes	70	10	-0.377	0.00192	0

Note 1. Acceleration set to 0.001 cm/sec^2 at 0.30 sec after impulsive settling.
Note 2. A fluorocarbon solvent registered by Minnesota Mining Mfg. Co.

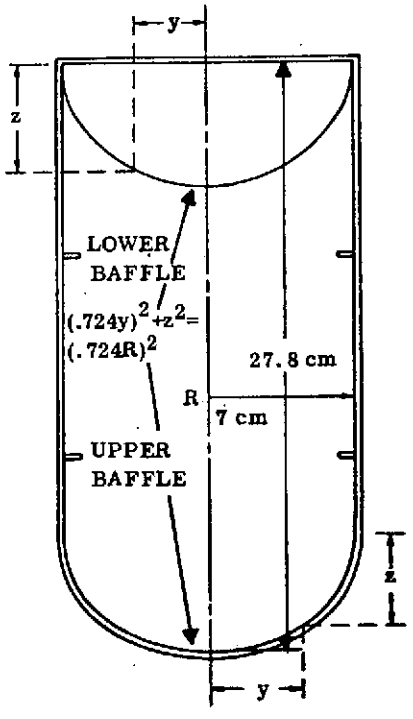

Figure 9. Drop Tower Model of LH_2 Fuel Tank

Certain additional procedures and variables were held constant for five cases and will be mentioned only here. The fluid velocities in the tank at initial time were always zero.

Free-slip boundaries were used in these simulations. Only one-half the tank was modeled in cylindrical coordinates, the centerline was the left boundary of the problem. A turbulent viscosity coefficient of 0.05 was recommended in Reference 3 and was used in all five cases. The value of kinematic surface tension for all cases in this study was zero. Although surface tension affects interface behavior and would be significant in Case 2 after the step change in acceleration, it is not important for predicting fluid motion for Bond numbers in excess of 100 used for settling in the cases in this study. The number of cells, particles, and the scaling factor will be discussed for individual cases.

The geometry for the drop tower models was taken from Ref. 9 and is shown in Figure 9. It was used without baffles

for Cases 1 and 2, while Cases 3, 4 and 5 were all run with baffles. Additional information is given in Figure 10, the D-1T geometry. However, identical ellipsoidal bulkheads of the geometry of the aft bulkhead in the fuel tank were used both forward and aft for all cases rather than the D-1T conical forward bulkhead. Case 2 was identical to Case 1 geometry except for a scaling factor of 5.5/7.0 which was used. Cases 4 and 5 were identical to 3 so a scaling factor of 152.4/7.0 was used for the full-scale cases.

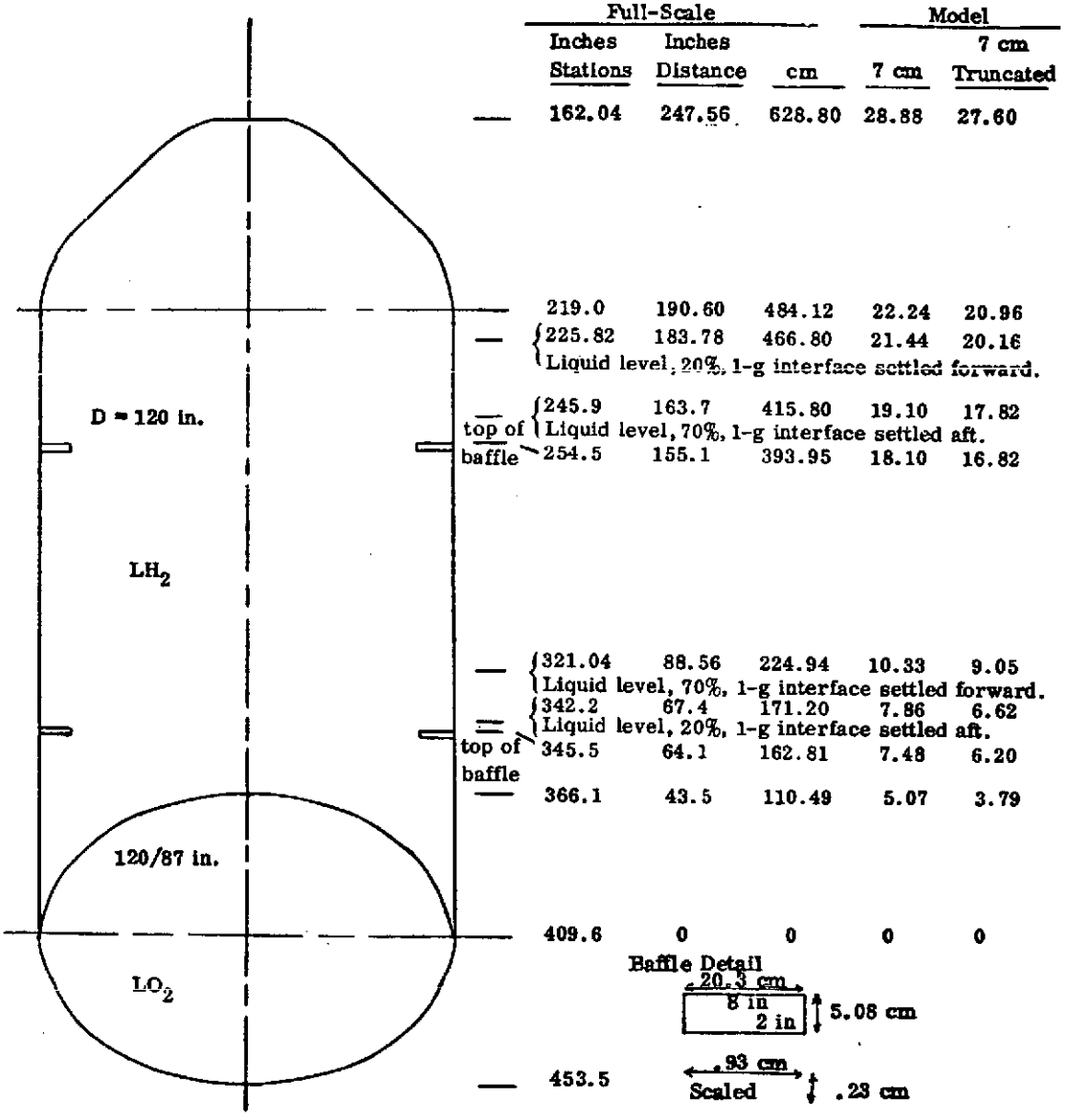

Figure 10. D-1T Tank Configuration With Full-Scale and Model Dimensions

3.1 DROP TOWER MODEL CORRELATIONS

Three drop tower cases were simulated to verify program modeling of flow phenomena. These cases were only run long enough to accomplish this objective.

3.1.1 MODEL CASE 1. This case was setup with the new Code ERIE to compare the simulation with a known analytical model case and verify the change over to a variable grid. The 20% liquid Case 3 results from the previous study were used for this comparison (Ref. 2, 3). This 288-cell problem with 1772 particles had a rectangular grid 1 cm by 1 cm. All variables and conditions were maintained consistent with the earlier Case 3 to provide this comparison. This included a surface tension value of zero.

The results of the new code were nearly identical to the earlier code through 0.75 seconds simulation, comparable leading edge velocities were obtained. These velocities agreed closely with those predicted by $v = 0.87\ g_z t$ from the results of LeRC drop tower correlations (Ref. 9); departure from the free-slip condition can only be explained by turbulent and viscous dissipation. Differences in some individual cell velocities were resolved to be actual differences in the code. The results to 0.925 seconds are presented in Figures 11 and 12. Since the primary purpose of this task was a verification of the code, the run was stopped at 0.925 sec. It is important to point out two significant differences which were experienced in bottom bulkhead flow behavior. Different program logic was employed in turning the flow in the lower right corner, this resulted in lower velocity flow across the bulkhead and a thicker particle layer than experienced in Reference 3. Finally, the initial centerline geyser velocities are lower than previous HOPI results which were too high; these results are reasonably close to the values experienced in drop tower tests. The separation of marker particles in the corner area of Figure 11G was noted, however, it was not considered necessary to correct this in the coarse grid comparison problem.

The comparison between the drop tower motion picture sequence and the similar time sequence from code ERIE for Case 1 shows very similar flow phenomena occurring. The leading edge in Figure 13B is slightly ahead in the computer code but the agreement is very good. In Figure 13D at time 0.90 seconds, the flow is observed to be on the bottom bulkhead and ERIE also reflects a wetted bulkhead with very similar flow patterns. The ERIE code sequence ends at 0.925 seconds whereas the photograph 13D shows the geyser slightly further advanced at 0.95 seconds. The above comparison indicates excellent agreement between the two sequences.

3.1.2 MODEL CASE 2. An impulsive-g drop tower case was modeled with a settling acceleration of -73.5 cm/sec^2 applied for 0.30 seconds with a reduction to $+0.001$ cm/sec^2 comparable to drag for the duration of the run. This 65% liquid case was modeled with a grid of 400 cells and 2772 particles. The container was 5.5 cm in radius and was scaled from the 7 cm grid configuration. A denser particle region was used in the earliest area to show motion to insure marker particle spacing did not become so sparse

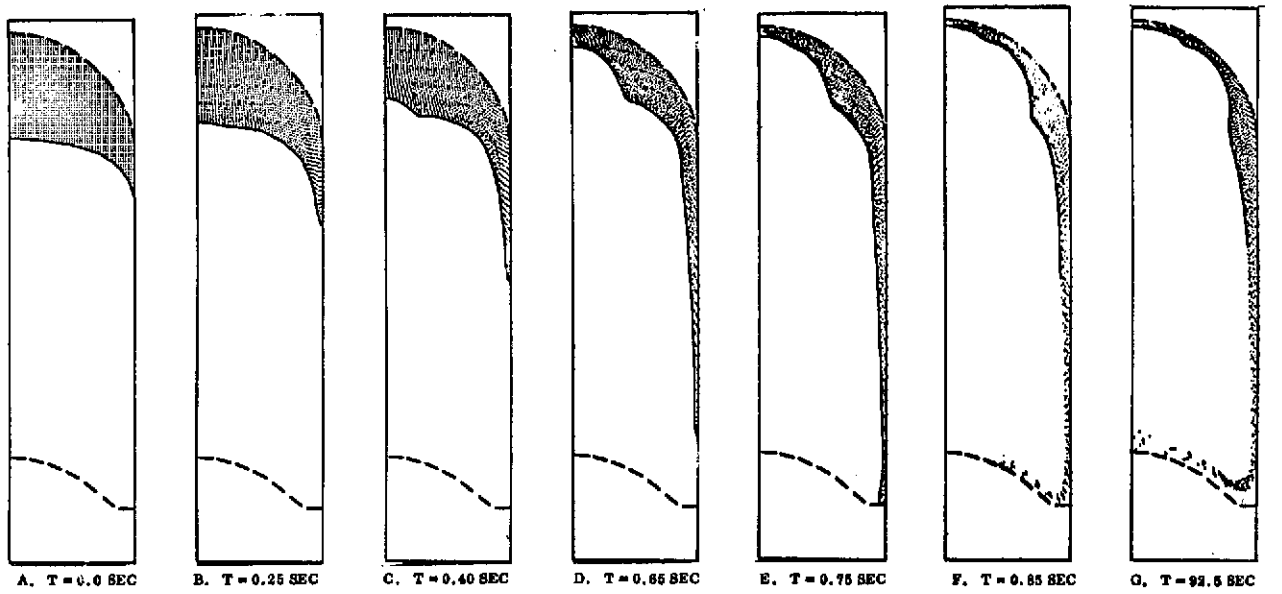

Figure 11. Marker Particle Plots for Drop Tower Model - Case 1

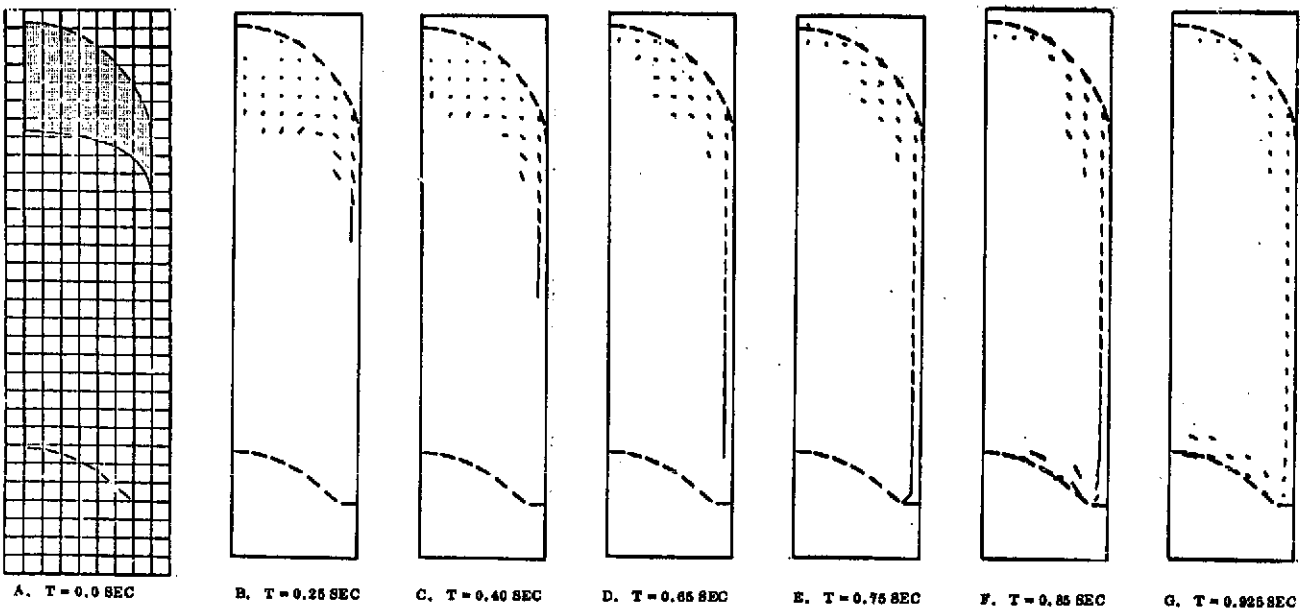

Figure 12. Velocity Vector Plots for Drop Tower Model - Case 1

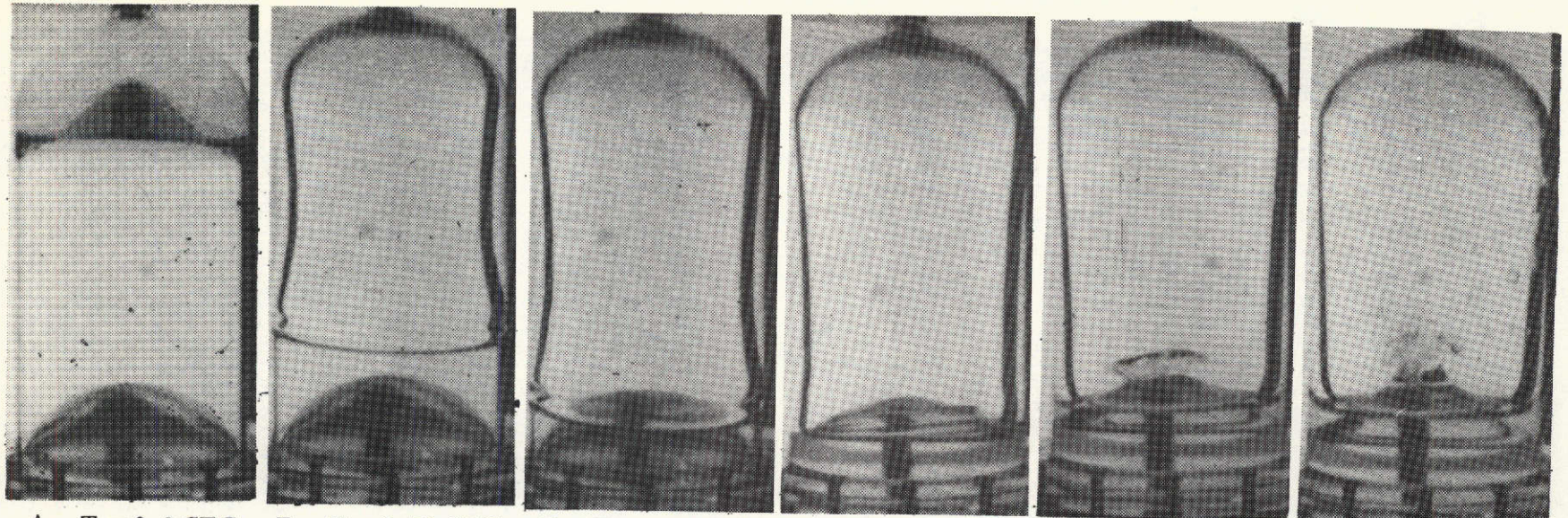

A. T = 0.0 SEC B. T = 0.70 SEC C. T = 0.80 SEC D. T = 0.90 SEC E. T = 0.95 SEC F. T = 1.00 SEC

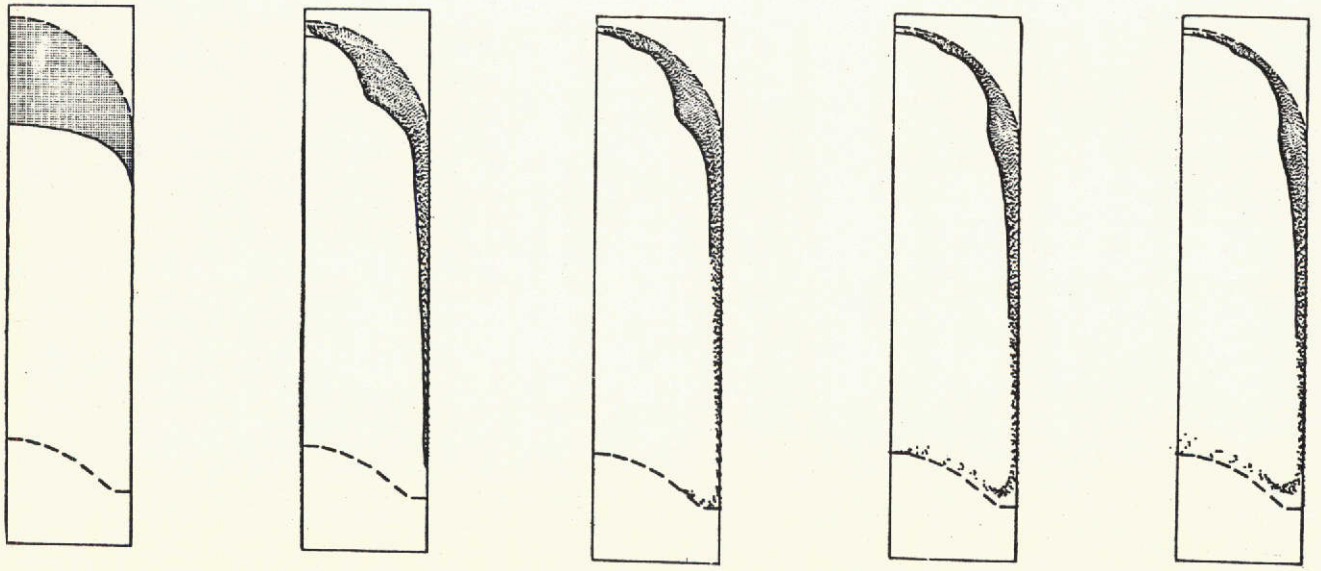

A. T = 0.0 SEC B. T = 0.70 SEC C. T = 0.80 SEC D. T = 0.90 SEC E. T = 0.925 SEC

Figure 13. Motion Picture Results Compared With ERIE Simulation for Drop Tower Model - Case 1

as to indicate empty cells which should be full. The problem was started with a kinematic surface tension of 28.3 cm^3/sec^2, however the erroneous surface pressures and unusual results caused us to go back to a zero surface tension value for the remainder of the cases in this study. Surface tension affects interface behavior and would be important after the step change to very low-g in this case.

The particle and vector plots are shown in Figures 14 and 15 for the first 0.35 seconds of this impulsive-g simulation. Convergence difficulties occurred at this time and the run could not be continued. A velocity and pressure field adjustment was observed to occur at about this time in earlier runs (Ref. 3) containing a high percentage of liquid, therefore the non-convergence after several hundred iterations cannot definitely be attributed to the change in g-level. Further work with the relaxation parameter (Equation 25) is required to determine a method of reducing the iterations. This capability to vary g-level in a step manner had been verified in a problem with less head effect during program checkout. Nonetheless, the inability to model this case within the budget allowed was most dissappointing. Methods to correct it such as changing the time step, changing the coefficient of relaxation in the convergence scheme, modifying the g-level change to a ramp, and increasing the number of iterations all failed to yield desired results. This problem area requires further attention; the problem should be run without a perturbation in acceleration to verify any effect of pressure-velocity changes on convergence at this problem time.

3.1.3 MODEL CASE 3. This model case was the first of the baffle cases and represents the geometric configuration for later full-scale D-1T settling cases. Thus it was the most important of the three model cases. The drop tower model was simulated with a grid of 422 cells and used 843 particles spaced at uniform density. The initial configuration is shown in Figures 16A and 17A. The interface configuration was obtained from a cross plot of z/R versus Bond number with x/R as a parameter from data for cylindrical containers available in Reference 10. With this initial set-up and a flat interface representing a Bond number of 15, an interface instability occurred at the centerline. This was corrected by altering the interface shape at the centerline and changing the configuration of the initial grid. Other velocity definition problems occurred due to small cells near the centerline which received extremely high velocities on empty cell faces due to their dimensions and location at the centerline; the ratio of cell-center radial location affects the velocities set to satisfy divergence. Whereas small δr cells may be desirable to study centerline geysers, they produce very high velocities which result in small time steps in problems with radial flow resulting from baffles. As indicated above, the final selected grid is shown in Figure 17A with fine cells in the vicinity of the baffles and lower right corner and larger radius cells at the centerline. This configuration proved satisfactory and no centerline instability problem was observed. The marker particle and velocity vector plot sequence for this settling case is shown in Figures 16 and 17. The flow leaves the baffle at about 0.3 seconds and flows toward the centerline. Velocity of departure from the baffle is nearly 10 cm/sec. The significance of this velocity is discussed in more detail below. The fluid clears the top of the tank at 1.05 second. A minor secondary geyser forms at the centerline

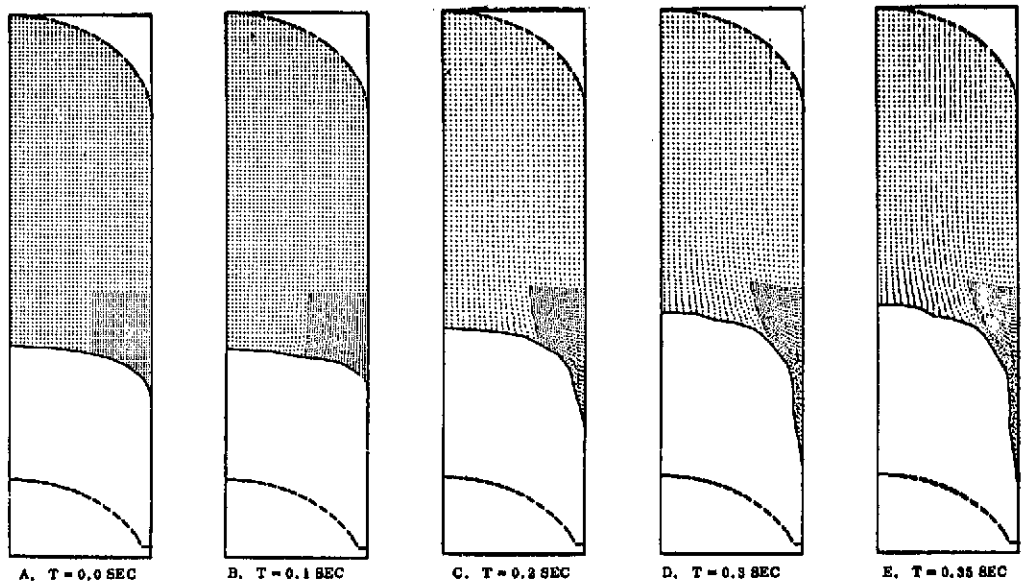

Figure 14. Marker Particle Plots for Drop Tower Model - Case 2

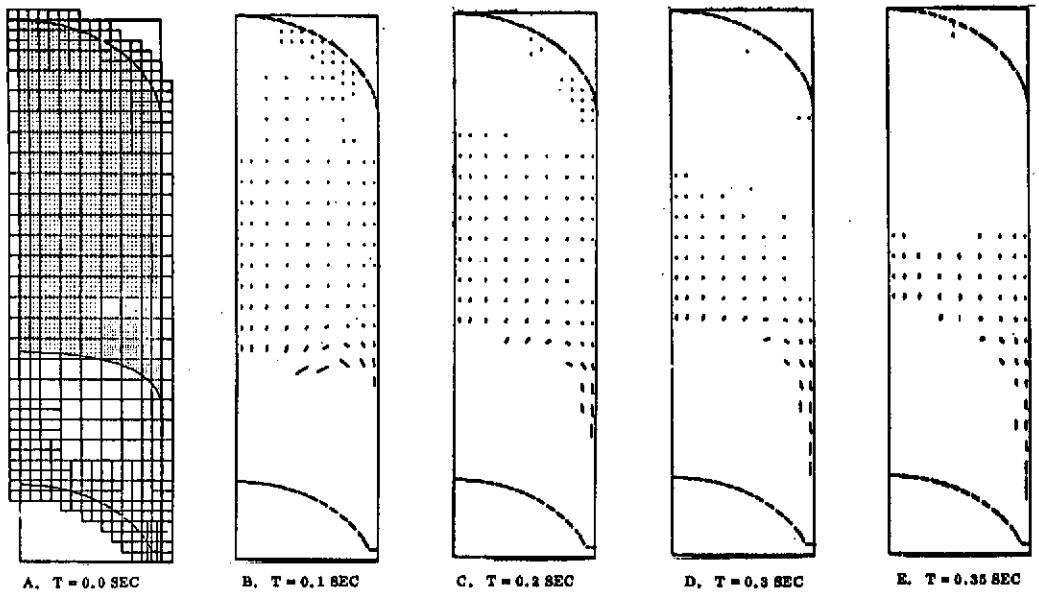

Figure 15. Velocity Vector Plots for Drop Tower Model - Case 2

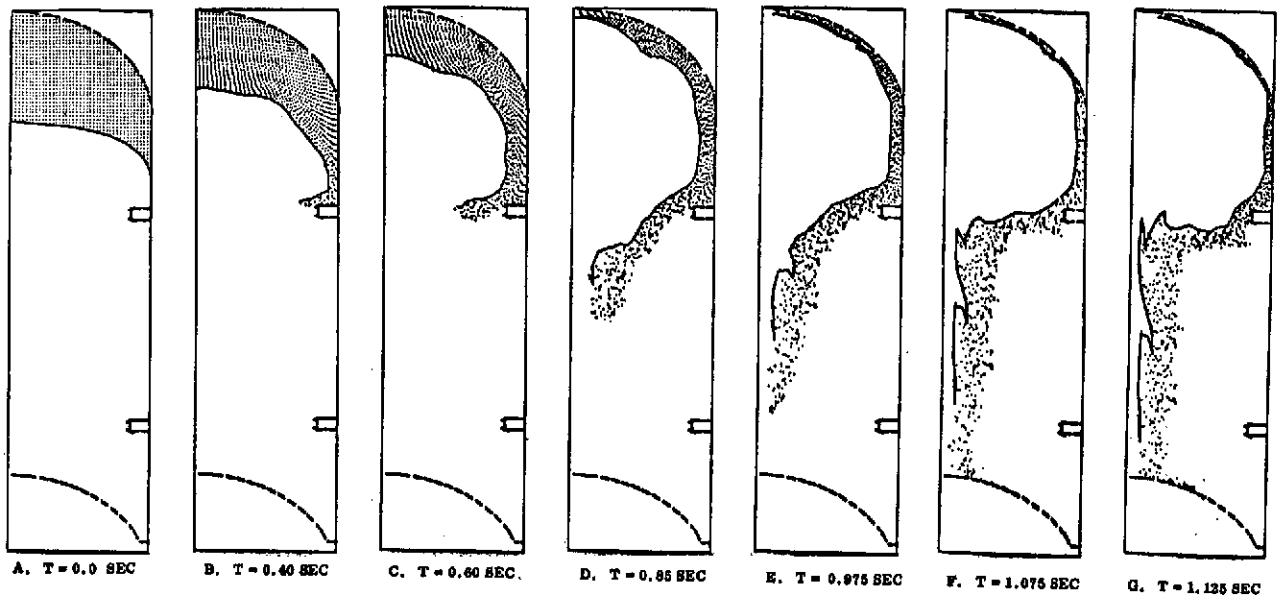

Figure 16. Marker Particle Plots for Drop Tower Model - Case 3

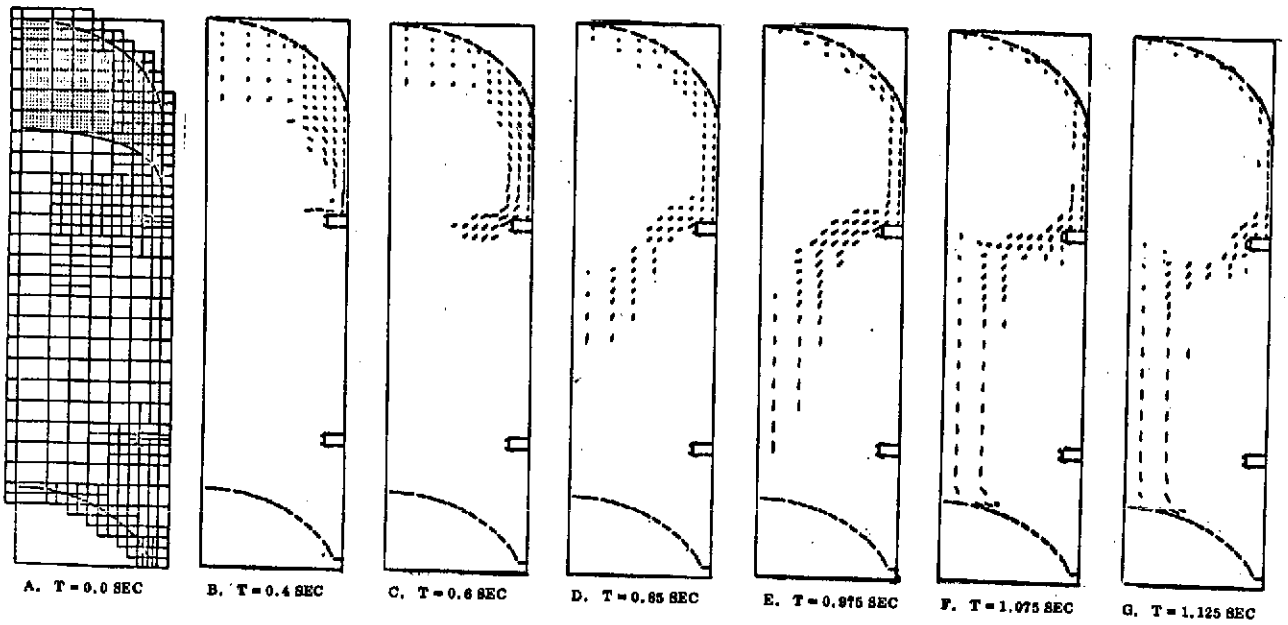

Figure 17. Velocity Vector Plots for Drop Tower Model - Case 3

at 1.075 sec (Figures 16F and 17F), however, this is a much weaker geyser than the centerline geyser observed in the drop tower film. A lower initial velocity off the baffle is a possible explanation for this behavior.

Nevertheless, the flow representation in ERIE was in good agreement with the free-fall velocity simulation of the drop tower model. It was not necessary to continue this run beyond 1.075 sec since the ability to model this configuration was established and the full-scale Case 4 represents the same geometry and fill-level. The motion picture sequence for this simulation of drop tower results is presented with Case 4, the comparable full-scale simulation.

A brief investigation into the effect of the magnitude of the radial velocity component leaving the upper baffle was stimulated by the results of Case 3 where drop tower results indicated a higher axial impingement location than code ERIE determined. The drop tower indicated the flow to come off the baffle and reach the centerline causing a secondary geyser which covered the vent area; whereas code ERIE results did not reflect this.

An analytical approach, a simplified trajectory model, was suggested by Rouse (Ref. 11). This analysis is complicated by the model geometry. The flow is off of a ring baffle in a cylinder, therefore the radial flow area is continually diminishing and the flow must be either thickening or accelerating if both continuity and momentum conservation are to be observed. It is offered that increased turbulence probably results in a loss of momentum in the radial as well as the axial direction. Marker particle plots and drop tower movies confirmed that the radial velocity is nearly constant and a definite thickening of the leading edge is detectable. A literature review on this subject led to an article authored by Strelkoff and Moayeri which contains a rigorous solution to the overall problem (Ref. 12). Their discussion of the phenomena is enlightening, however, the application of their solution is beyond the scope of this study. A parametric analyses of trajectories as a function of velocity off the baffle was developed for both the model and the full-scale case and are presented in Figures 18 and 19. It will be pointed out later that velocities off the baffle in full-scale Case 4 were near 5 cm/sec. The point of flow convergence at the centerline or on the bottom bulkhead is sensitive to this initial velocity, which in itself is a function of the initial fluid position above or on the baffle and the resulting vertical flow length which the fluid flow experiences. Any initial downward velocity would further contribute to a higher velocity off the baffle. The trajectory is obviously most sensitive to the absolute value of axial acceleration. The results of this analysis support the favorable comparison of drop tower fluid behavior with that observed in the model simulation case 3C.

The drop tower initial velocities were possibly higher due to initial conditions and resulted in flow reaching the centerline higher in the tank. Again referring to Figures 18 and 19, the simplified model makes no allowance for spreading of the jet and simply assumes a particle trajectory moving radially inward and axially downward.

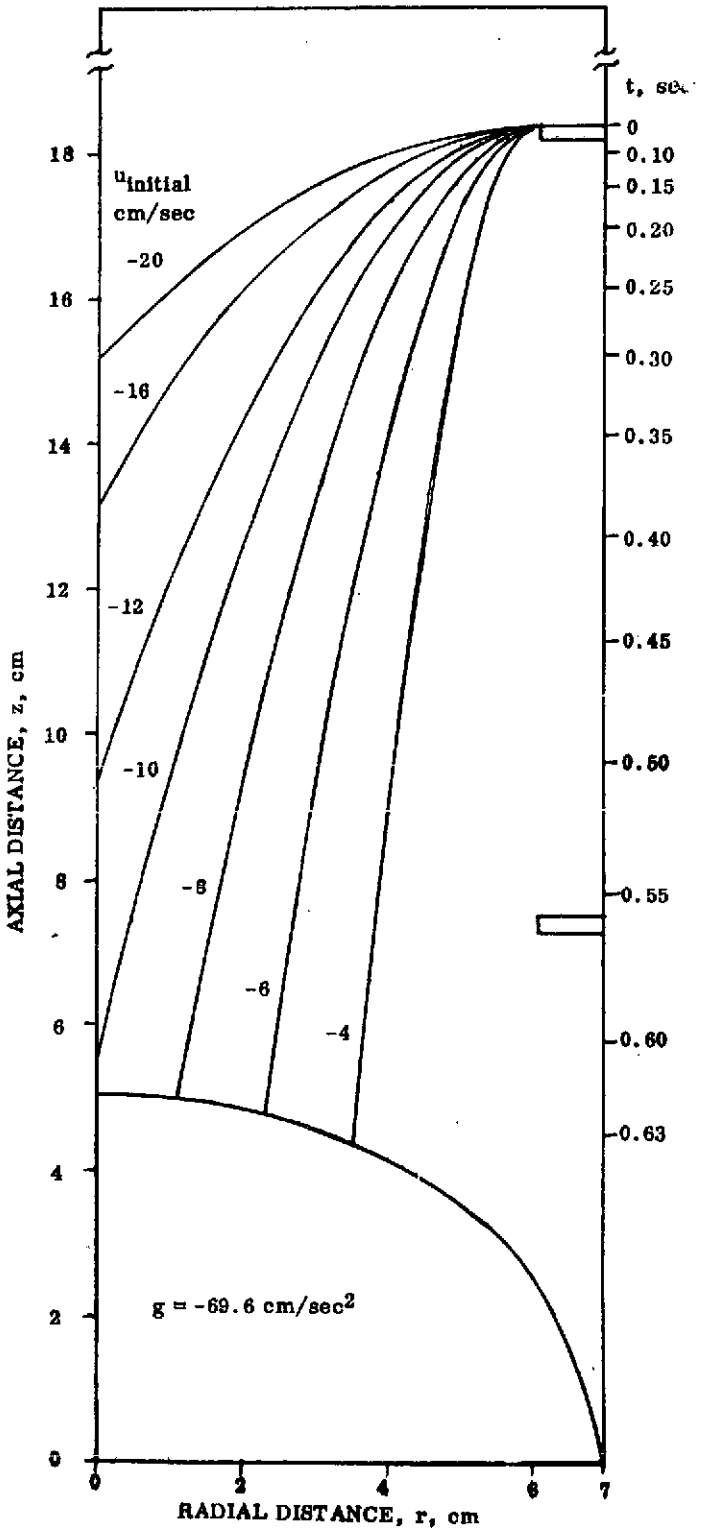

Figure 18. Particle Trajectory for Simplified Math Model of Drop Tower Baffle Overfall - Case 3

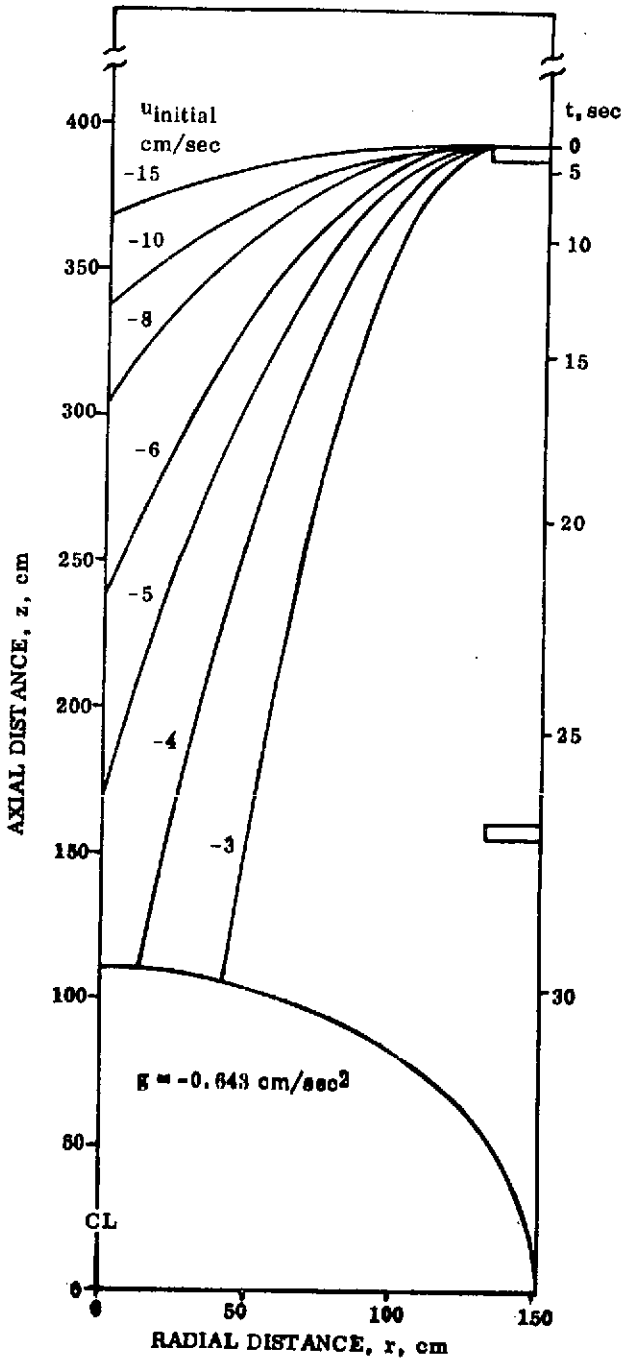

Figure 19. Particle Trajectory for Simplified Math Model of Full-Scale D-1T Baffle Overfall - Case 4

Comparisons of Case 3 with Figure 18 indicate the validity of the simplified model. For Case 3, fluid left the baffle at a velocity of 12 cm/sec at about 0.40 sec problem time and the model predicts reaching the centerline some 0.50 sec later (0.90 problem time) and reaching the bulkhead 0.62 sec later (1.02 sec problem time). Figure 16 justifies that these numbers are reasonably valid.

For Case 4, a similar analysis using 5 cm/sec initial radial velocity with a departure at the baffle lip of 10 sec real time predicts centerline impact 25 seconds later (35 sec real time) and bottom bulkhead impact 30 seconds later (40 sec real time). Figure 20 verifies the close similarity to the ERIE code results for the full-scale case. Note that when particles reach the centerline and it is flagged full, this essentially represents centerline impact. The centerline boundary condition surpresses apparent impact of the particles on the left boundary.

3.2 FULL-SCALE CORRELATIONS

Two full-scale cases were analyzed simulating the settling of residual LH_2 prior to the third (Case 5) and fourth (Case 4) venting operations of the Centaur D-1T Proof Flight. The respective liquid residuals for these restarts are approximately 70 percent and 20 percent liquid. The configuration is shown in Figure 10. It is a scaled version of model Case 3 with a scale factor of 21.77. The thrust for settling for each restart is constant, thus the respective settling accelerations are 0.377 and 0.643 cm/sec^2. The initial Bond numbers representing drag are 10 and zero, respectively.

3.2.1 FULL-SCALE CASE 4. This full-scale simulation of the D-1T fuel tank with 20 percent liquid was simulated with a 422 cell grid with 843 particles. The initial Bond number of zero resulted in the fluid initially wetting the upper baffle before settling started. A zero Bond number was simulated with a hemispherical interface. The initial configuration for Case 4 is shown in Figure 20A. The complete settling sequence is shown in Figures 20 and 21; the liquid was collected below the bottom baffle at run termination of 120 seconds although sloshing and vapor clearing persisted.

Horizontal velocities off the upper baffle ranged from 2.5 to 3.5 cm/sec. This agrees with the anticipated lower velocities for the full-scale case. This velocity confirms the expected fluid impingement point at the centerline from Figure 19. The fluid reaches the centerline prior to impact with the bottom bulkhead; i.e., the left most row of cells are all FUL. Radial velocities of zero on the centerline preclude movement of particles closer than occurs in Figure 20. The fluid impacts the bottom bulkhead and flows down the bulkhead into the lower right corner. It rebounds from this corner and impacts the bottom side of the lower baffle. The fluid then continues to mix below the bottom baffle with only minimal geysering behavior occurring thereafter.

The top area of the tank in the vicinity of the vent clears at approximately 55 seconds and is followed by fluid falling below the top baffle. The secondary geyser which momentarily formed near the bottom bulkhead at the centerline dissipates briefly after

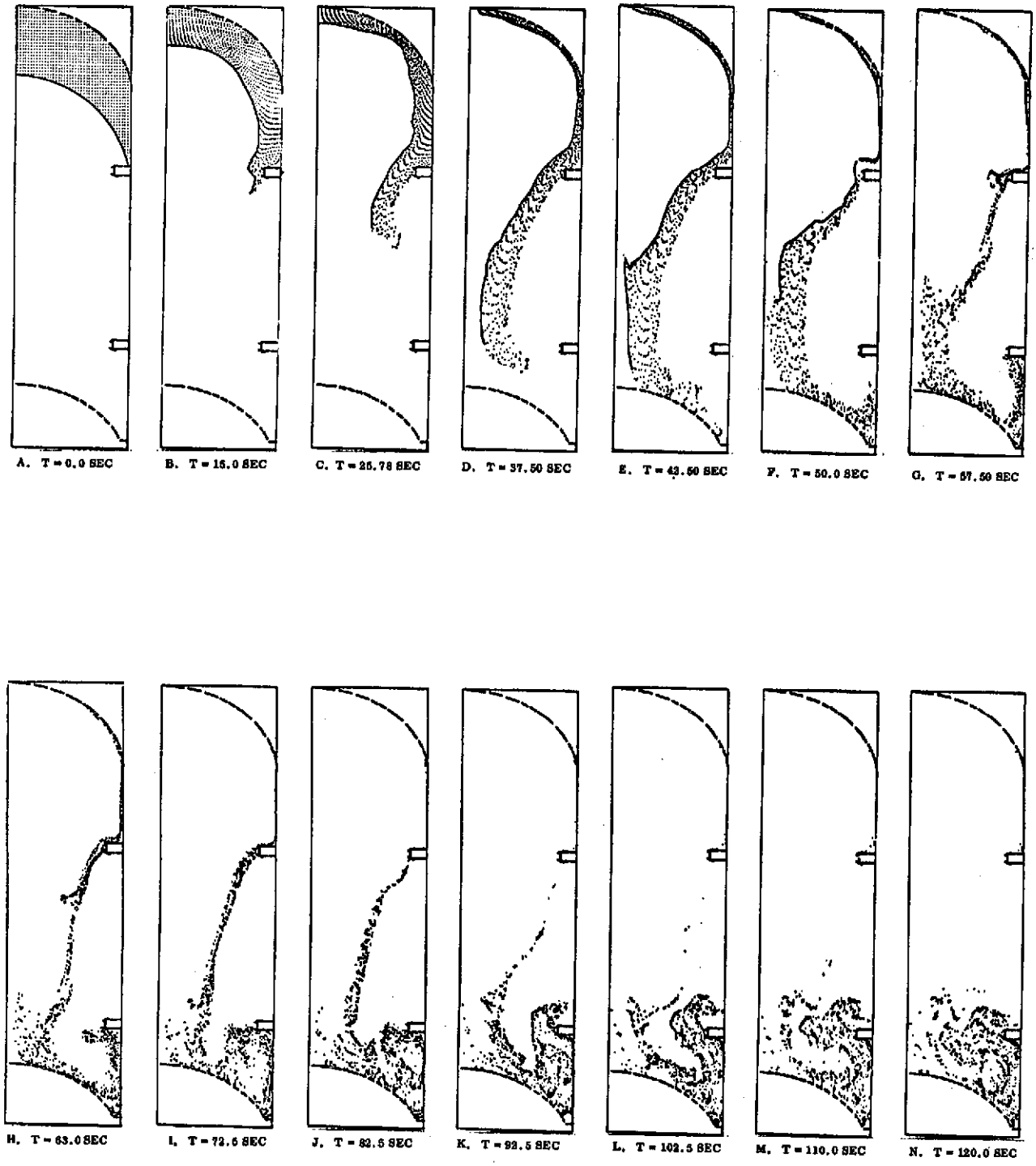

Figure 20. Marker Particle Plots for Full-Scale D-1T Simulation - Case 4

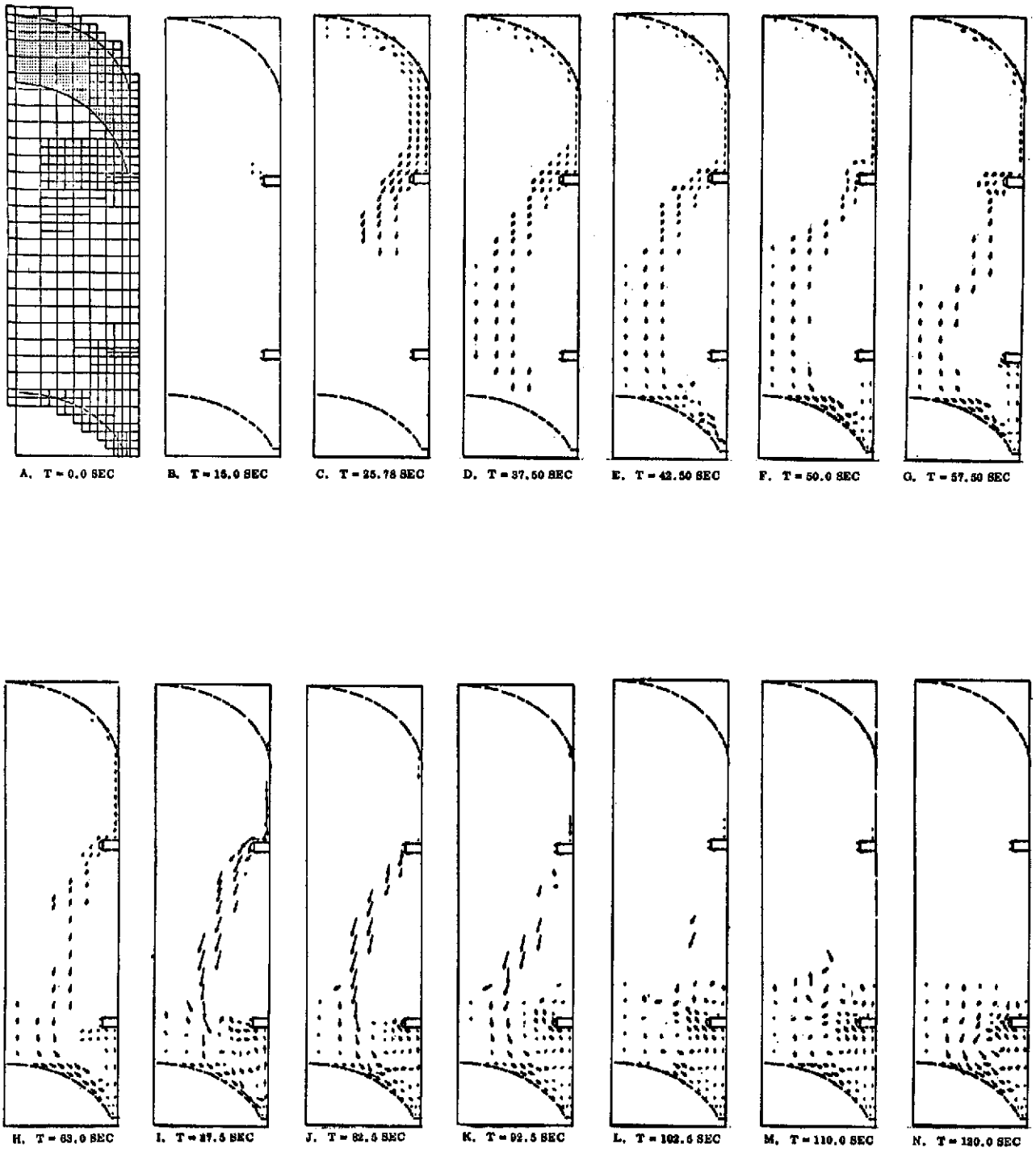

Figure 21. Velocity Vector Plots for Full-Scale D-1T Simulation - Case 4

initiation. A vortex flow develops in the lower right corner dissipating energy through turbulence and leaving a volume which contains bubbles and vapor voids.

The settled liquid below the lower baffle flows upward around the lower baffle but at very low velocities in comparison with settling flow velocities nearer the center of the tank. The velocity vector plots at 82.5 seconds in Figure 21J indicate all cells below the baffle to be full even though particle plots indicate sparse areas. Plots at 92.5 seconds indicate flow patterns above the lower baffle; these are turning laterally and are in the process of settling toward the tank bottom. This suggests the liquid is essentially collected at this time. Although an apparent trough exists below the baffle, the cell size is of such a magnitude that these cells are flagged full for all times after 90 seconds. The significant developments during this period 90 to 120 seconds include the clearing of fluid from cells higher than the second row above the baffle and a decay in the maximum fluid velocities in the collected liquid. The maximum velocity in the liquid decreased from 5.1 cm/sec at 115 seconds to 4.6 cm/sec at 120 seconds. It is also significant that by 120 seconds all interface velocities are in a negative or downward direction. It is observed that the vortex flow below the baffle continues to lose energy through turbulent dissipation and no further fluid interface disturbances will result.

The D-1T Proof Flight plan calls for a 5-1/4-hour coast period with 20 percent liquid residual prior to fourth burn. If venting is required during this period, the propellant will be cleared from the vent area with 12 lb settling thrust for a period of 180 seconds followed by a 40-second vent period at 24 lb thrust. For the fourth MES, a 420-second settling sequence is used, 300 seconds at 12 lb thrust and 120 seconds at 24 lb thrust. Venting is permitted for 24 seconds commencing at -120 seconds. These settling times exceed the times determined in Case 4 by a factor of two to three; this assures adequate time for the emergency of bubbles from the collected liquid and for the decay of slosh in a low-gravity field.

The settling sequence in Figure 22 compares a NASA/LeRC model drop tower sequence to the full-scale Case 4 sequence for D-1T Proof Flight. Accelerations for the two sequences are -69 and -0.643 cm/sec^2 respectively. The first drop tower photograph is at 0.475 sec where the liquid has flowed over the baffle, impacted with radial flow at the centerline, and resulted in a geyser rising to foul the vent area. Similar flow behavior was absent in the Case 4 full-scale simulation. The remainder of the squence shows additional comparisons of flow phenomena. This example emphasizes the importance of full-scale modeling since the flow trajectories off the baffle are significantly different between the drop tower model simulation and the full-scale simulation. Maintaining the Bond number constant as you change the scale factor from 1 to 20 may well not duplicate flow conditions with baffles because of the complexity of the flow dynamics.

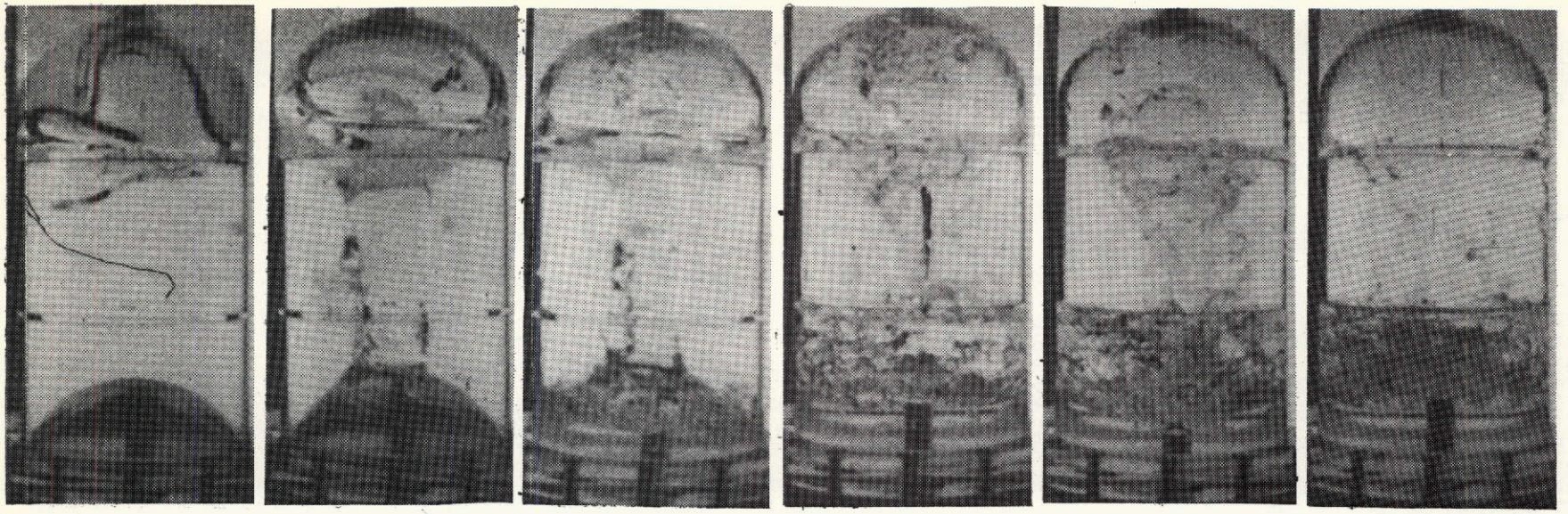

A. T = 0.475 SEC B. T = 0.875 SEC C. T = 1.06 SEC D. T = 1.29 SEC E. T = 1.66 SEC F. T = 2.21 SEC

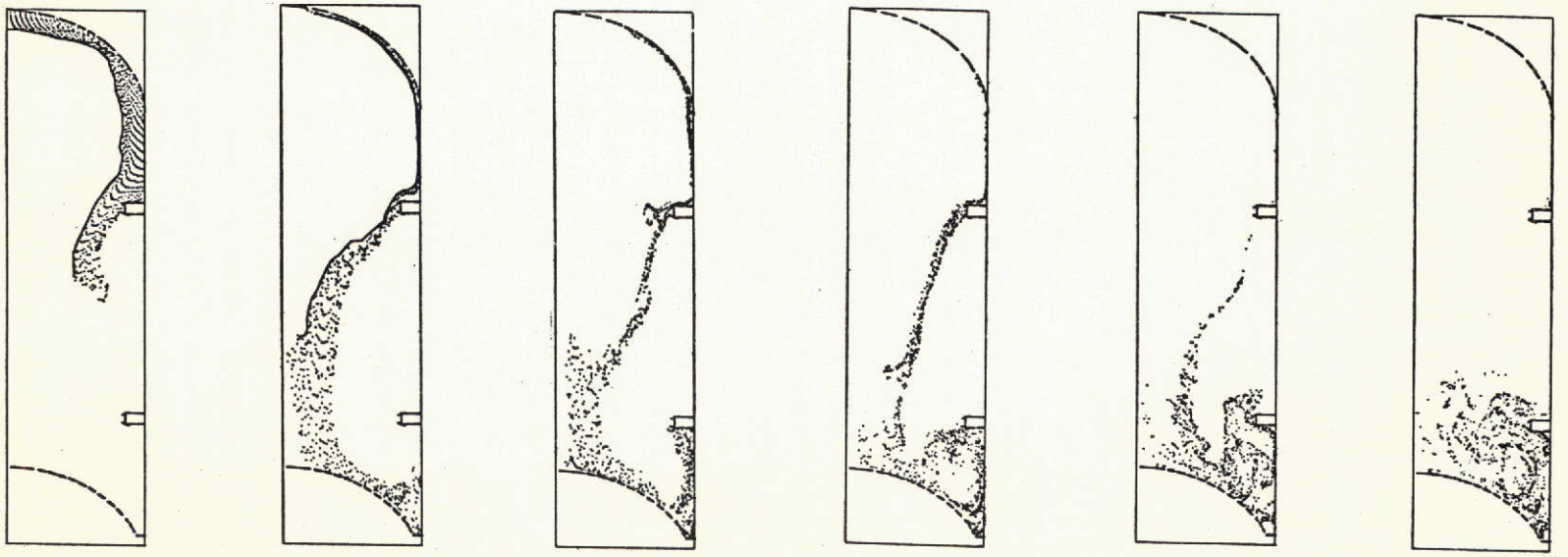

A. T = 26.0 SEC B. T = 47.5 SEC C. T = 57.5 SEC D. T = 70.0 SEC E. T = 90.0 SEC F. T = 120.0 SEC

Figure 22. Motion Picture Results Compared With ERIE Simulation for D-1T - Case 4

3.2.2 FULL-SCALE CASE 5. The final simulation case was a D-1T fuel tank with 70 percent liquid. This was modeled with a 416 cell grid with 3085 particles spaced with uniform initial density. The grid was modified from Case 4 to place finer grid mesh near the lower baffle, however arbitrary boundaries and external tank configuration remained the same. The initial Bond number was ten with the initial fluid position slightly above the lower baffle. The initial fluid configuration is shown in Figure 23A.

In this simulation case, with about half the gravity of Case 4 and a slightly longer liquid run prior to hitting the baffle, the fluid comes off with primarily a minus u-component velocity and nearly reaches the centerline prior to falling under the effect of gravity. Interestingly, the point of impact on the bottom baffle is not too different for the Cases 4 and 5. A well-defined geyser developes at the centerline at 60 seconds and moves upward dissipating at 80 seconds. The flow across the bottom bulkhead is as anticipated and when the lower baffle is impacted from below, a vortex forms which entraps vapor. The flow off the lower baffle begins to turn upward at 60 seconds commencing to fill this portion of the tank. At approximately 100 seconds, the volume below the baffle is full. The centerline geyser falls back toward the lower baffle creating complex flow patterns in this area. The upper door and vent area in Case 5 clears of liquid at about 120 seconds. In Figure 24N at 155 seconds, the maximum velocity below the lower baffle is less than 2.5 cm/sec. The velocity vectors in Figure 24 are particularly clear in establishing the flow pattern; from 120 to 150 seconds they indicate a well-defined flow pattern above the lower baffle. A secondary geyser has formed at the centerline, however the settling thrust is sufficient to retard the upward velocity and stall the flow. The surface velocities of the centerline cells are indicative of this. For times of 140, 145, 150 and 155 seconds, the upward velocity is observed to decay from 7.09 cm/sec to 5.07, 3.19, and finally to 1.73 cm/sec, respectively. This decay rate indicates the geyser will soon roll back in a slosh wave. The upward momentum of this cylindrical section of fluid is substantially less than its downward counterpart near the wall. The baffles will be beneficial in this energy decay process. In the time steps of 145, 150, and 155 seconds, the maximum tank velocity occurring vertically midway between the ring baffles dropped from 7.5, 6.8, to 4.6 cm/sec, respectively. This final collected liquid configuration is in an essentially stable situation and no significant geyser action is expected. This again can be contributed to the baffles dissipating energy and to the continuous applied settling thrust.

The D-1T Proof Flight plan settling procedures for the 80-minute coast period prior to third burn, 70 percent liquid, calls for a 350 second, 12 lb thrust settling period if venting is required. This precedes the venting period of 40 seconds at 24 lb thrust. The 350 seconds alloted by the Proof Flight for the venting sequence is adequate in view of results obtained in this study. As indicated in Case 4, the results here indicate severe fluid motion has died out however settling times larger than this assure removal of bubbles and slosh dampening prior to venting.

The above simulation results in Cases 4 and 5 for the two full-scale cases are most promising. They indicate positive clearing of the vent area and an absence of any

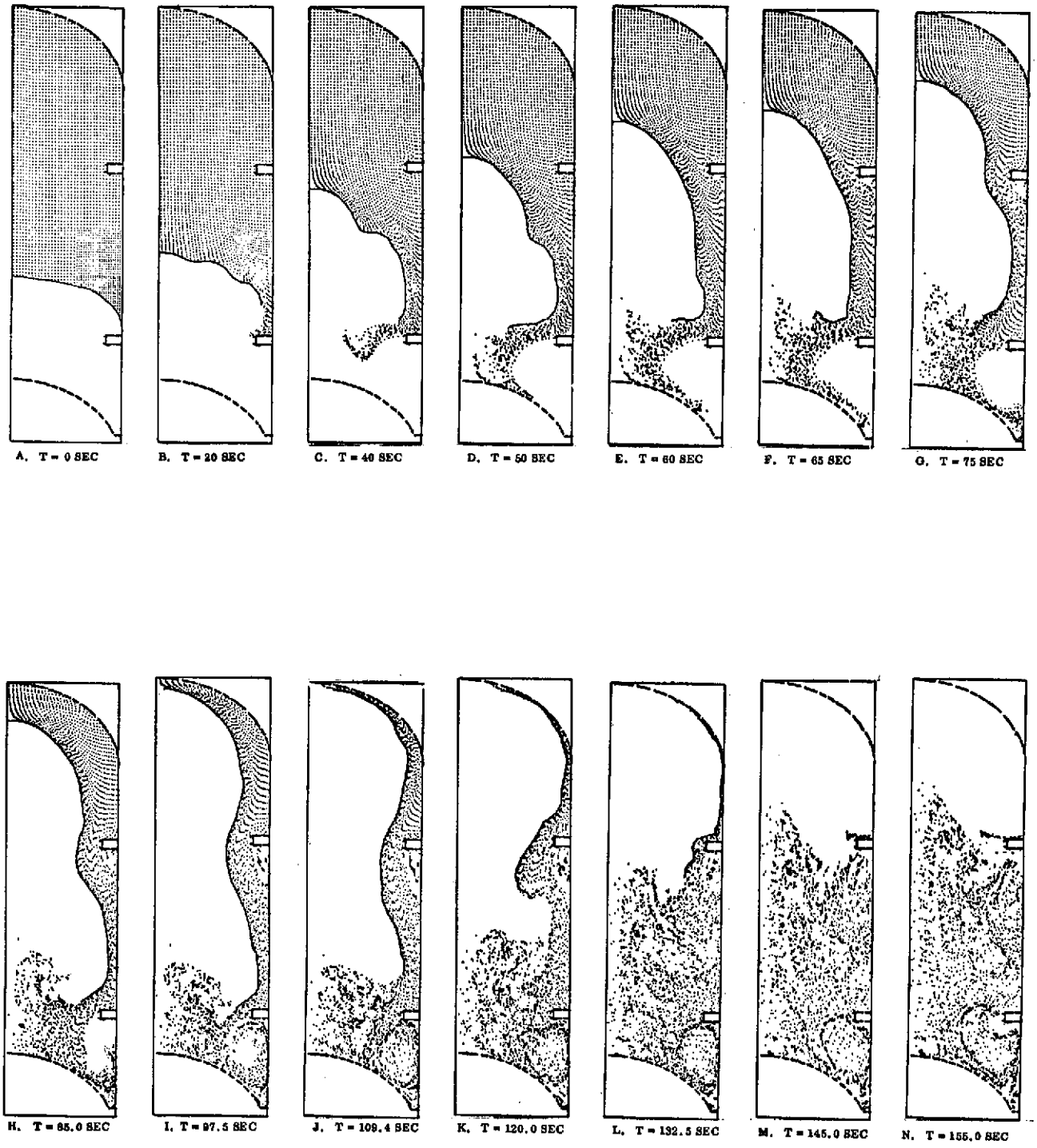

Figure 23. Marker Particle Plots for Full-Scale D-1T Simulation - Case 5

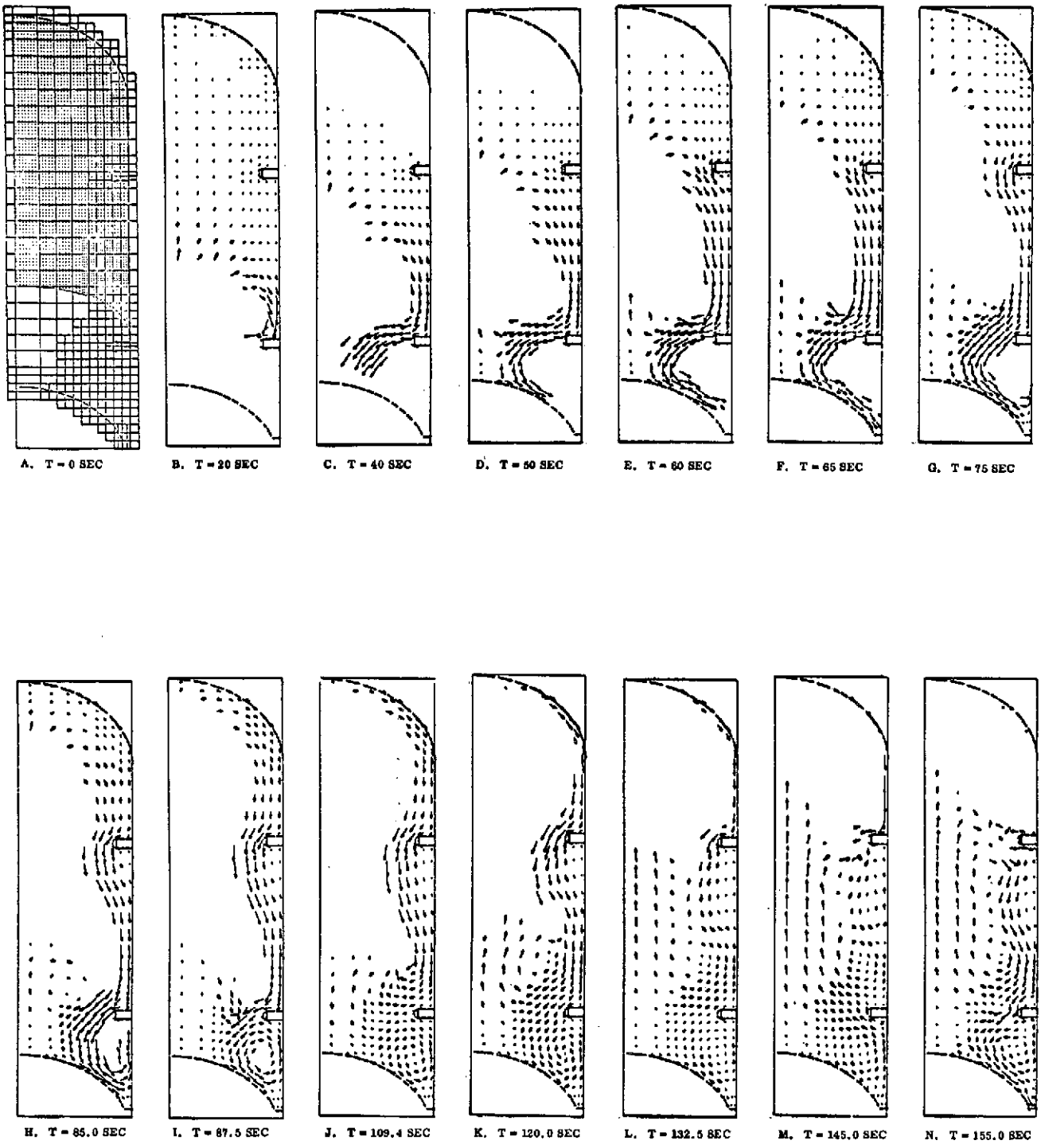

Figure 24. Velocity Vector Plots for Full-Scale D-1T Simulation - Case 5

secondary geyser which fouls the vent area. Both cases were simulated for sufficient times to indicate collected liquid. Both cases illustrate the effectiveness of the lower ring baffle in surpressing the geyser which occurs after impact with the bottom bulkhead.

3.3 D-1T INSTRUMENTATION

It is anticipated that the D-1T Proof Flight early in 1974 will yield flight data which can be assessed to confirm the results of the full-scale simulations. The third burn is preceded by an 80-minute coast with 70 percent liquid while the fourth and final burn is preceded by a 5-1/4-hour coast with 20 percent liquid residual. An instrumentation location diagram is shown in Figure 25 to indicate the locations of the available instrumentation. A total of 16 liquid-vapor sensors and three ullage temperature sensors are included in the Centaur D-1T proof flight fuel tank. Additionally, seven skin temperature patches are included. Times which can be defined will include the wetting of the lower baffle, the drying out of the vent area and the drying out in the upper baffle area for Case 4. The baffles and the instrumentation sensors are pictured in Figure 26 and 27. The Centaur fuel tank door with its two vent ports is shown in Figure 28.

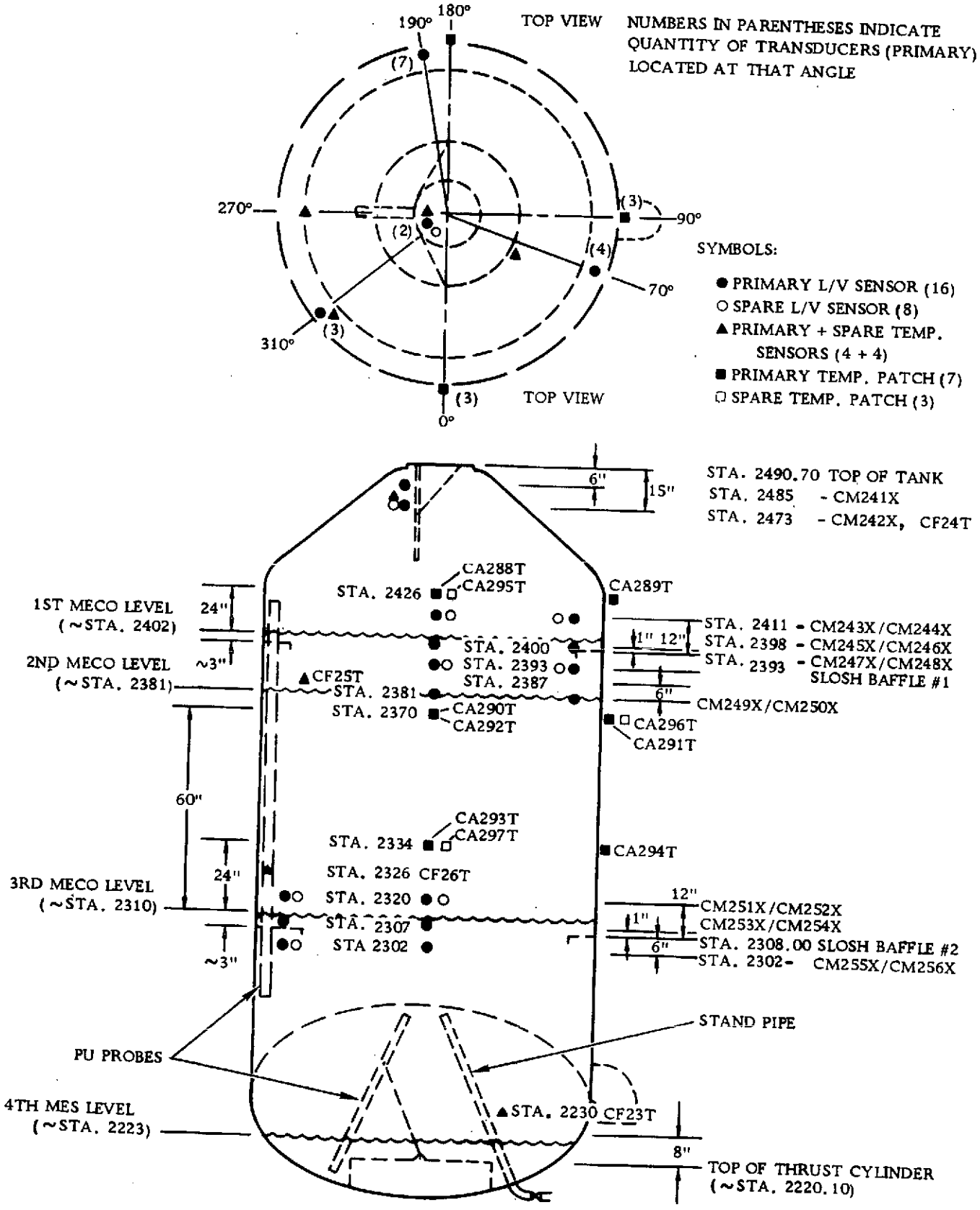

Figure 25. Centaur D-1T Propellant Tank Flight Instrumentation Locations

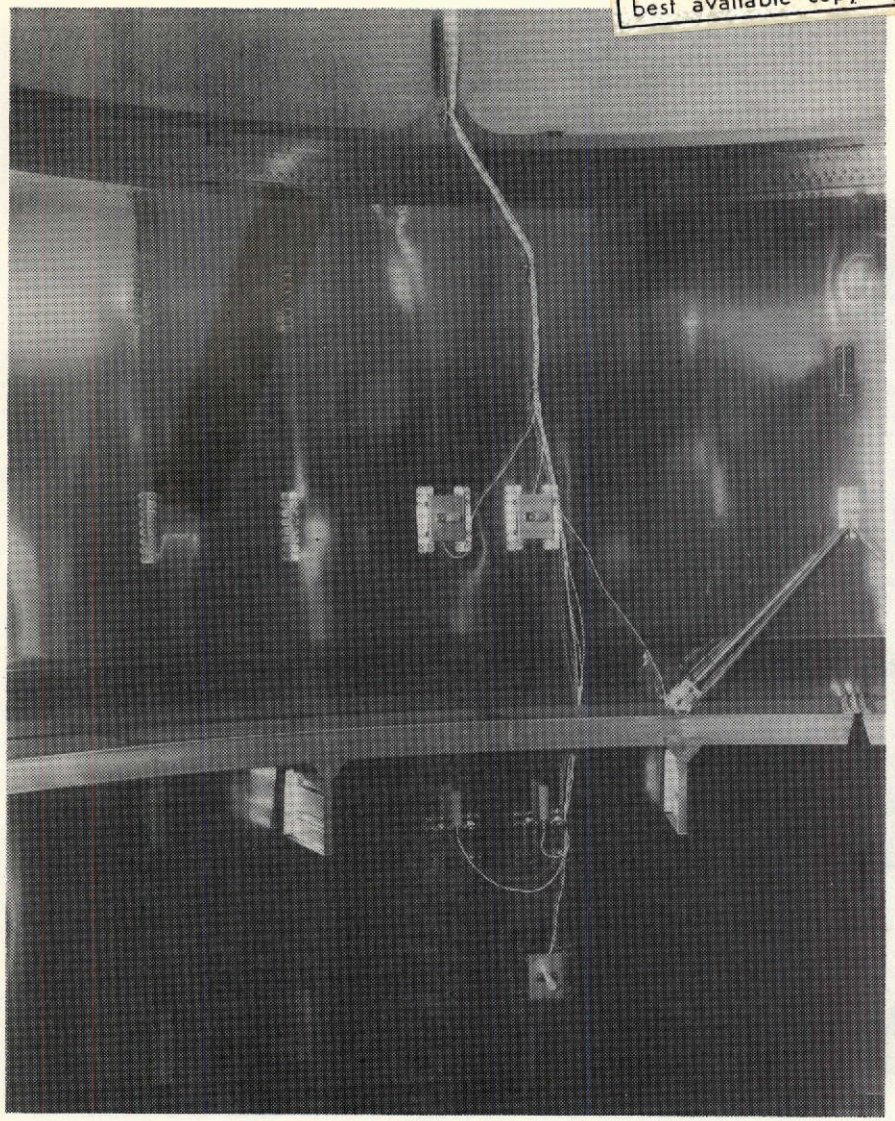

Figure 26. Upper Baffle and D-1T Flight Instrumentation Liquid-Vapor Sensors

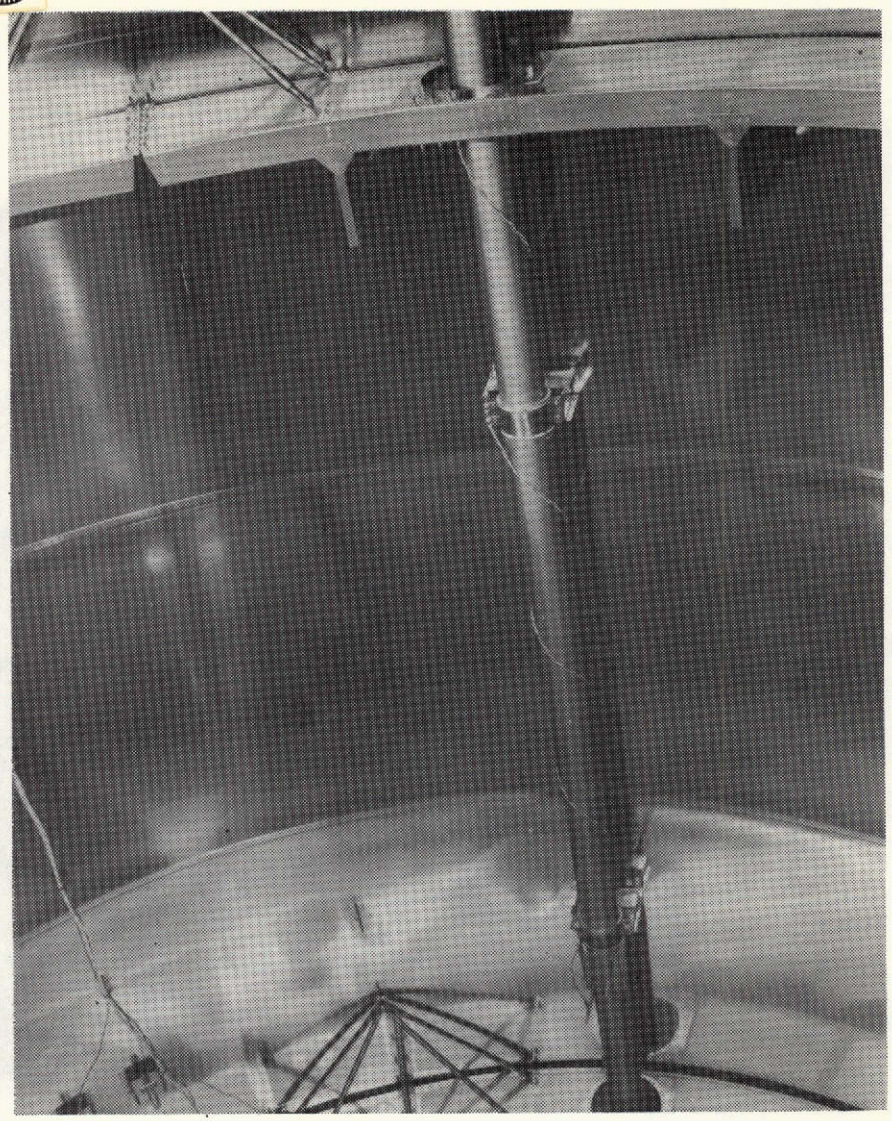

Figure 27. Upper Baffle and D-1T Flight Instrumentation Suspended Off PU Probe

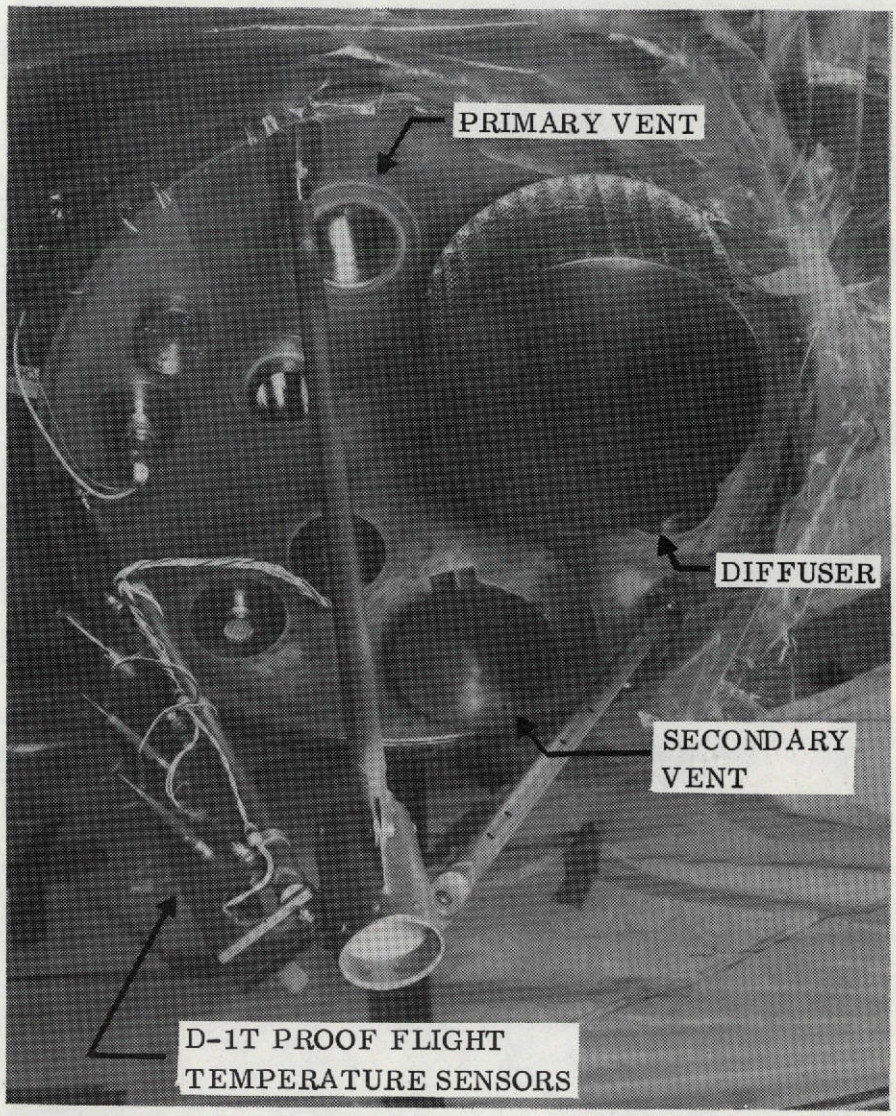

Figure 28. Centaur D-1T Fuel Tank Upper Door Showing Vents and Diffuser

4.0 CONCLUSIONS AND RECOMMENDATIONS

The simulation of Lewis drop tower model cases demonstrated the validity of the new variable grid mesh version of the computer code. The variable grid improved the flow resolution along the walls, in the corners, and facilitated modeling of baffles. The simulation of flow dynamics produced good agreement with drop tower results. Calculated times for clearing the vent area and collecting the liquid closely duplicated model results.

The full-scale results for simulating flow dynamics for clearing the vent area and collecting the liquid for Centaur D-1T Proof Flight confirmed the extrapolation of drop tower data. It further indicated the importance of full-scale modeling to achieve accurate initial conditions and to implement the use of absolute magnitudes of acceleration. For 70 and 20 percent residuals, numerical results indicated vent clearing to occur at 120 and 55 seconds while collected liquid condition existed after 155 and 120 seconds, respectively.

The five simulation cases pointed out the importance of modeling initial interface conditions for flow off of a baffle. Significantly different trajectories result for different velocities over the baffle. Accurate modeling is important since higher velocities cause flow impingement at the centerline resulting in secondary geysers which foul the vent area and increase time to collect liquid. The computer simulations indicated less geyser phenomena than occurred in drop tower tests.

The results of reorientation flow from this study illustrate the complex flow phenomena which is not necessarily amenable to drop tower modeling. Therefore, full-scale simulation with a computer code such as ERIE is required. Some differences in fluid behavior were apparent in the scale-up from Case 3 drop tower simulation to Case 4 full-scale simulation. These results indicate that each particular case should be modeled full-scale since there are no universal examples of settling flow.

The modifications to the SMAC computer code to implement a variable grid and time-dependent axial gravity capability resulted in a valuable tool for analysis of reduced-gravity flow. Improved resolution of flow near walls and baffles resulted. Structured in overlay, this new code is twice as efficient in core usage as the previous version for the same problem size. Also, optimum use is made of the maximum allowable time step to increase efficiency. The largest problem in particle and cell requirements run in this study, Case 5, had a maximum core requirement of 117223 octal. However, three quarters of the problem time spent in iteration requires only a core usage of 67670 octal. Case 5 used 4.6 hours central processer time on the CDC Cyber 70 and involved a computer cost of $2750.

It is recommended that additional work in this important area of reduced gravity flow simulation be continued with the computer code ERIE now available and verified. The interface behavior during settling flow is of interest, especially for low Bond number reorientation flow. The surface tension capability in VGSMAC should be verified prior to using ERIE to simulate this particular flow behavior. This verification would provide a capability to correctly model surface behavior in variable-g settling. Variable-g settling offers a potential savings in the total impulse required to achieve the settled state.

Flow behavior in the vicinity of propellant tank start baskets or around and within the thrust barrel in the LO_2 tank for D-1T Centaur is of interest. The program could be used to indicate the flow behavior during filling for the thrust barrel for various liquid residuals and various settling accelerations.

The new code offers the potential to study inflow/outflow or tank mixing in a reduced gravity field with improved resolution not previously available for areas of important flow phenomena. Mixing flow patterns in tanks in reduced-gravity must be understood to optimize design of propellant management systems. Performance of a thermodynamic vent system in reduced-gravity could be analyzed.

Finally, additional program improvements are recommended. The flexibility to modify the grid without restarting the problem would provide a capability to examine specific areas in greater detail as the problem develops. Improved visibility of the flow phenomena could be gained with the ability to transfer marker and velocity vector plots to a continuous media of movie film.

APPENDIX A

NOMENCLATURE

Bo	Bond number, gR^2/σ
c	wave speed
D	velocity divergence = $(1/r^{\alpha})\ (\partial r^{\alpha}u/\partial r) + (\partial v/\partial z)$, distance
EPS	convergence criteria
G	cell flag
g_r	radial acceleration
g_z	axial acceleration
h	height of
$\hat{n}$	unit normal defining a boundary segment
P	pressure, L^2T^{-2}
r	radial coordinate
R	radial distance to center or side of cell determined by subscript
R_1, R_2	radius of curvature
t	time
u	radial component of velocity
$\tilde{u}$	radial storage variable, radial component of the tilde velocity
v	axial component of velocity
$\tilde{v}$	axial storage variable, axial component of the tilde velocity
$\vec{V}_M$	liquid velocity at midpoint of boundary segment computed with distance weighting interpolation scheme
x	horizontal coordinate in rectangular coordinate system
$\vec{X}_M$	position of midpoint of a boundary segment
$\vec{X}_p$	position of particle
y	vertical coordinate in rectangular coordinate system
z	axial coordinate in cylindrical coordinate system
α	geometric parameter, $\alpha = 1.0$ in cylindrical coordinates and equals 0.0 in plane (cartesian) coordinates

δr	incremental step in the r direction
δz	incremental step in the z direction
ϵ	boundary sensing parameter
λ	minimum mesh dimension, minimum of δr or δz
η	ratio of lengths in defining surface pressures
υ	kinematic viscosity, L^2T^{-1}
ξ	relaxation parameter
ϕ	true pressure normalized to unit density
σ	kinematic surface tension, L^3T^{-2}
ψ	arbitrary pressure normalized to unit density (pseudopressure), L^2T^{-2}
ω	vorticity

Superscripts

k	iteration index
n	time cycle index

Subscripts

N	identifier for primary cell under consideration
NL	left boundary of cell N
NB	bottom boundary of cell N

REFERENCES

1. Bradshaw, R. D.; and Kramer, J. L.: A Variable Grid SMAC Computer Code With Arbitrary Boundaries: ERIE. Convair Aerospace Report CASD-NAS-74-006, Contract NAS3-16772, February 1974.

2. Betts, W. S.: A SMAC Computer Code With Arbitrary Boundaries: HOPI. Convair Aerospace Report 632-1-85, NAS3-14361, 19 April 1972.

3. Betts, W. S.: An Analytical Study of Reduced-Gravity Liquid Reorientation Using a Simplified Marker and Cell Technique. NASA CR-120944, Convair Aerospace Report GDCA-DDB72-003, NAS3-14361, August 1972.

4. Amsden, A. A.; and Harlow, F. H.: The SMAC Method: A Numerical Technique for Calculating Incompressible Fluid Flows. Los Alamos Scientific Laboratory Report No. LA-4370, 17 February 1970.

5. Bowman, T. E.: Sheet of Liquid Flowing Down a Wall. The Physics of Fluids, Volume 14, Number 7, July 1971, pp 1578-1579.

6. Salzman, J. A.; and Masica, W. J.: Experimental Investigation of Liquid-Propellant Reorientation. NASA TN D-3789, 1967.

7. Viecelli, J. A.: A Computing Method for Incompressible Flows Bounded by Moving Walls. Lawrence Radiation Laboratory Report UCRL-72815, September 1970.

8. Amsden, A. A.: Numerical Calculation of Surface Waves: A Modified ZUNI Code With Surface Particles and Partial Cells. Los Alamos Scientific Laboratory Report No. LA-5146, May 1973.

9. Salzman, J. A.; Masica, W. J.; and Lacovic, R. F.: Low-Gravity Reorientation in Scale-Model Centaur Liquid-Hydrogen Tank. NASA TN D-7168, February 1973.

10. Hastings, L. J.; and Rutherford, R.: Low Gravity Liquid-Vapor Interface Shapes in Axisymmetric Containers and a Computer Solution. NASA TM X-5379, October 7, 1968.

11. Rouse, H.: Elementary Mechanics of Fluids. John Wiley and Sons, Inc., 1946.

12. Strelkoff, T.; and Moayeri, M. S.: Patterns of Potential Flow in a Free Overfall. Journal of Hydraulic Division, Proceedings of the American Society of Civil Engineers, Volume 96, pp 879-901, April 1970.